

Constraining the Interiors of Asteroids Through Close Encounters

Jack T. Dinsmore,^{1*} Julien de Wit²

¹*Department of Physics, Massachusetts Institute of Technology*

²*Department of Earth, Atmospheric, and Planetary Science, Massachusetts Institute of Technology*

Accepted XXX. Received YYY; in original form ZZZ

ABSTRACT

Knowledge of the interior density distribution of an asteroid can reveal its composition and constrain its evolutionary history. However, most asteroid observational techniques are not sensitive to interior properties. We investigate the interior constraints accessible through monitoring variations in angular velocity during a close encounter. We derive the equations of motion for a rigid asteroid’s orientation and angular velocity to arbitrary order and use them to generate synthetic angular velocity data for a representative asteroid on a close Earth encounter. Using Markov Chain Monte Carlo fits, we perform injection-retrieval tests on these synthetic data to gain insights into the extent to which interior properties can be constrained. We also perform a sensitivity analysis of such an inversion technique to asteroid parameters (e.g., asteroid shape and orbital elements), observational set-up (e.g., measurement precision and cadence), and mapping models to convert constraints on the density moments to density distributions. We find that high precision in rotational period estimates (order of tens of milliseconds to seconds) are necessary for each cadence, and that low perigees ($\lesssim 18$ Earth radii) are necessary to resolve density distributions.

Key words: minor planets, asteroids: general – methods: data analysis – planets and satellites: interiors

1 INTRODUCTION

Over the past twenty years, the increase in quantity and quality of sensitive all-sky surveys has prompted the discovery of numerous asteroids. Such advances have been made via ground-based surveys such as the Catalina Sky Survey [Larson et al. \(1998\)](#), Pan-STARRS [Kaiser et al. \(2002\)](#), and the Lincoln Near-Earth Asteroid Research project (LINEAR) [Stokes et al. \(2000\)](#), as well as space-based instruments such as the Wide-field Infrared Survey Explorer (WISE) mission [Wright et al. \(2010\)](#). Many of these asteroids are relatively small, but some are kilometre-sized and a few are predicted to closely encounter Earth or other planets in the near future. More encounter candidates are likely to be discovered by new efforts such as the Large-aperture Synoptic Survey Telescope (LSST) [Tyson \(2002\)](#). Their encounters can then be monitored by global ground-based networks such as the Las Cumbres Observatory (LCO) [Brown et al. \(2013\)](#). Such ground-based monitoring is typically used to derive the rotation period of an asteroid and its surface properties (see e.g. [Devogèle et al. \(2021\)](#)).

Since the tidal torque acting on an asteroid during an encounter depends on the interior mass distribution, the careful monitoring of angular velocity variations during an encounter also presents a window into the interior properties of asteroids. The gravitational two-body system has been studied in

the context of tidal torque to different orders and with several different methods [Paul \(1988\)](#); [Scheeres et al. \(2000\)](#); [Ashenbergs \(2007\)](#); [Boué & Laskar \(2009\)](#); [Hou et al. \(2017\)](#). Further theoretical studies showed that the tidal torque, observed through angular velocity perturbations, is sensitive to asteroid interior density distribution [Naidu & Margot \(2015\)](#); [Makarov et al. \(2022\)](#); [Scheeres et al. \(2004\)](#).

Angular velocity perturbations have been observed and used to extract asteroid properties in several cases, including for the 2013 encounter of (367943) Duende with Earth [Moskovitz et al. \(2020\)](#); [Benson et al. \(2020\)](#), and asteroid binaries (3905) Doppler and (617) Patroclus [Descamps et al. \(2020\)](#); [Berthier et al. \(2020\)](#). Orbital and physical properties, including moment of inertia (MOI) ratios have also been extracted for asteroid 99942 Apophis, discovered on June 19, 2004 by R. A. Tucker, D. J. Tholen, and F. Bernardi [Giorgini et al. \(2005, 2008\)](#); [Smalley et al. \(2005\)](#), and on target to encounter Earth in 2029 [Yu et al. \(2014\)](#); [Hirabayashi et al. \(2021\)](#); [Valvano et al. \(2022\)](#); [Lee et al. \(2022\)](#). However, density distribution features beyond the MOI ratios have not yet been extracted for any asteroid encounters. More research is needed to study in what cases these effects are observable, and what factors generally inhibit observation of these new features. It seems pivotal to augment previous work on the effect of tidal torque on Apophis’ angular velocity in particular [Souchay et al. \(2014, 2018\)](#) so that upcoming observations may constrain these properties and thus improve our predictions.

We address this community need by developing a method-

* E-mail: jtd@stanford.edu

ology to translate (1) time series of asteroid angular velocity data into constraints on density moments and (2) constraints on density moments into constraints on an asteroid’s density distribution. Other techniques, such as measurement of tidal distortion Richardson et al. (1998), impact or seismometry experiments Richardson et al. (2005), or gradiometry Carroll & Faber (2018), may additionally constrain the density distribution. In section 2, we introduce the analytical and numerical fundamentals of this methodology. There, we describe a simulation used to integrate the equations of motion and produce synthetic data of angular velocity over time, followed by a Markov Chain Monte Carlo (MCMC) fit process which extracts density moments from the fit data. We then describe two methods to generate full density distributions from the density moments. In section 3, we present the results of a series of injection-retrieval tests demonstrating the extent to which the properties of an asteroid chosen to generate synthetic spin data can be retrieved via our methodology. Finally, in section 4, we assess the sensitivity of these constraints to various physical, observational, and methodological parameters to provide guidance for monitoring upcoming close encounters.

2 METHODS

In the following mathematical model for the influence of tidal torque on asteroid encounters, we assume for simplicity that (1) that the central body is much more massive than the asteroid, (2) that both are rigid, (3) that there are no distant perturbing objects and (4) that the asteroid is in a short-axis, non-tumbling rotational state before the encounter. All of these assumptions except 2 can be relaxed without drastic changes to the model.

The only properties of an asteroid’s density moments that affect tidal torque interactions are its “density moments,” defined here as

$$K_{\ell m} = \frac{a_A^{2-\ell}}{I_A} \int_A d^3r \rho_A(\mathbf{r}) R_{\ell m}(\mathbf{r}). \quad (1)$$

These are complex, unitless quantities. $\rho_A(\mathbf{r})$ is the asteroid density distribution and $R_{\ell m}$ are the regular solid spherical harmonics (see appendix A for details). The integral is computed over the entire asteroid mass, denoted A , and d^3r indicates the three-dimensional volume element throughout the paper. I_A denotes a MOI scale defined as

$$I_A = \int_A d^3r \rho_A(\mathbf{r}) r^2 \quad (2)$$

while a_A is the length scale

$$a_A^2 = \frac{1}{V_A} \int_A d^3r r^2 \quad (3)$$

where V_A is the asteroid volume. We call these MOI and length scales in part because they obey $I_A = \mu_A a_A^2$ for uniform asteroids where μ_A is the mass of the asteroid. Note that a_A is a function only of the surface of the asteroid, so that a_A is known if the surface is observed.

The tidal torque experienced by an asteroid is

$$\begin{aligned} \tau = & G \frac{I_A I_B}{2a_A^2 a_B^2} \left[\sum_{\ell m} a_B^\ell J_{\ell m} \sum_{\ell' m'} a_A^{\ell'} S_{\ell+\ell', m+m'}(\mathbf{D})^* (-1)^{\ell'} \right. \\ & \times \sum_{m''=-\ell'}^{\ell'} \sqrt{\frac{(\ell'-m'')!(\ell'+m'')!}{(\ell'-m')!(\ell'+m')!}} \mathcal{D}_{m'm''}^{\ell'}(\alpha, \beta, \gamma)^* \\ & \times \left. \left((i\hat{\mathbf{x}} - \hat{\mathbf{y}})(\ell' - m'' + 1) K_{\ell', m''-1} \right. \right. \\ & \left. \left. + (i\hat{\mathbf{x}} + \hat{\mathbf{y}})(\ell' + m'' + 1) K_{\ell', m''+1} + 2im'' \hat{\mathbf{z}} K_{\ell'm''} \right) \right], \end{aligned} \quad (4)$$

where \mathbf{D} is the position of the asteroid; α , β , and γ are $z-y-z$ Euler angles expressing the orientation of the asteroid; $S_{\ell m}$ are the irregular solid spherical harmonics; and μ_B and a_B are the mass and radius of the central body while $J_{\ell m}$ are the density moments of the central body. Equation 4 is derived in appendix A, assuming a rigid asteroid and no distant third-body perturbations. This is a novel derivation and accurate to arbitrary order in D .

Since it is the angular acceleration of the asteroid that is observable, rather than the torque applied, we also compute the MOI of the asteroid around the principal axes:

$$\begin{aligned} I_x &= \frac{2}{3} I_A (K_{20} - 6K_{22} + 1) \\ I_y &= \frac{2}{3} I_A (K_{20} + 6K_{22} + 1) \\ I_z &= \frac{2}{3} I_A (-2K_{20} + 1). \end{aligned} \quad (5)$$

Note that all moments of inertia are proportional to I_A . Equation 4 indicated that tidal torque was also proportional to I_A . The Euler equations, giving angular acceleration in terms of moment of inertia and torque (equation A14), show that the angular acceleration of the asteroid is independent I_A . Thus, the observables do not depend explicitly on I_A .

Throughout the paper, we refer to the “inertial frame” (the frame in which the orbit is fixed) and the “body-fixed frame” (the frame in which the asteroid is fixed and in which $K_{\ell m}$, I_A , and a_A are computed), which are also defined in appendix A.

2.1 Simulation design

We built a publicly accessible, custom simulation in C++ to produce time series of angular velocity data during a close encounter with a central body. This simulation requires as initial data (1) the orbital parameters of the asteroid r_p (perigee distance) and v_∞ (hyperbolic excess velocity); (2) the cadence of angular velocity observation Δt ; (3) the central body moments $J_{\ell m}$, mass μ_B , and radius a_B ; (4) the initial asteroid angular velocity in the inertial frame Ω_0 ; (5) the asteroid length a_A and (6) the asteroid’s density moments $K_{\ell m}$ and initial Euler angle γ_0 . All parameters except (6) are assumed to be known to high accuracy. For example, Ω_0 could be extracted from pre-encounter light-curve data and a_A from a model for the asteroid’s surface using radar. The other two initial Euler angles α_0 and β_0 are required to be zero by the assumption of no initial tumbling.

We begin our simulation at $D = 10r_p$. Since the leading

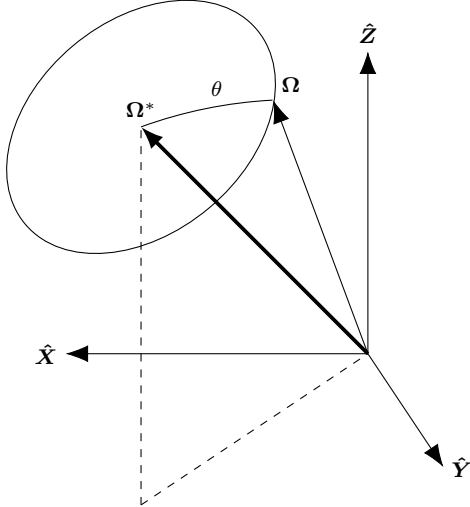


Figure 1. Diagram in the inertial frame of the uncertainty model used to define the probability that the true spin vector Ω^* should be observed as Ω . The angular uncertainty on θ and period uncertainty on $|\Omega|$ are treated separately.

order of the equations of motion is $\ell' = 2, \ell = 0$, this corresponds roughly to a torque of 10^{-3} times the maximum torque at perigee. Unless otherwise indicated, the simulation is terminated at $D = 10r_p$ as well.

With the simulation inputs specified, the equations of motion are integrated via the Runge-Kutta fourth order method, with a variable time step, chosen to limit integration error to only 100 times the floating point numerical error.

2.2 Uncertainty model

To add noise to data generated via the above simulation, we use the following uncertainty model. Each asteroid spin vector Ω is assumed to be uncorrelated with other spin vectors, and we model uncertainty in the orientation and in the period as also uncorrelated. Consider a true spin vector Ω^* . For the sake of description, we work in coordinates in which $\Omega^* \parallel \hat{z}$. Then, expressing the observed spin vector Ω in spherical coordinates, we draw the polar angle from a normal distribution with standard deviation σ_θ centred on zero and the azimuthal angle from a uniform distribution. We also draw the ratio Ω/Ω^* from a log-normal distribution centred on one, with width σ_P/P_ω , where $P_\omega = 2\pi/\Omega$ is the period of the asteroid. Explicitly, the probability density function (PDF) of P_ω is

$$P(\rho) = \frac{1}{\rho\sqrt{2\pi(\sigma_P/P_\omega)^2}} \exp\left(-\frac{\ln^2(\sigma_P/P_\omega)}{2(\sigma_P/P_\omega)^2}\right). \quad (6)$$

See figure 1 for an illustration of the uncertainty model. A log normal distribution is chosen such that $P_\omega > 0$, but since $\sigma_P/P_\omega \ll 1$ typically in our analysis, the probability distribution is essentially Gaussian.

The log likelihood resulting from this uncertainty model is

(excluding additive constants)

$$\ln \mathcal{L} = -\frac{1}{2} \sum_{i=0} \left[\frac{\cos^{-1}(\Omega_i^* \cdot \Omega_i / (\Omega_i^* \Omega_i))^2}{\sigma_\theta^2} + \frac{\ln(\Omega_i/\Omega_i^*)^2}{(\sigma_P/P)^2} + 2 \ln \frac{\Omega_i}{\Omega_i^*} \right]. \quad (7)$$

where Ω_i is the i th spin vector in the data set.

This model was chosen because it separates spin pole and period uncertainty. Therefore, if one is more precisely determined by measurement, σ_θ and σ_P/P can be adjusted separately in accordance.

2.3 Extracting density moments from spin data

Given synthetic data, an Affine Invariant MCMC Ensemble sampler was used to generate Posterior Probability Distributions (PPDs) from flat priors. We use the Python implementation `emcee` Foreman-Mackey et al. (2013). Our parameters were γ_0, K_{20}, K_{22} , and K_{3m} (10 in total), bounded by $|\gamma_0| < \pi/4$, and the K_{2m} bounds given in equation A5. Computing K_{3m} for many positive density distributions revealed a $|K_{3m}| \lesssim 0.01$, so we use more conservative bounds on K_{3m} of $|K_{3m}| < 1$. In general, spin data is most sensitive to γ_0 and K_{2m} , which we call the “first-order parameters.” We call K_{3m} the “second-order parameters.”

The MCMC was determined to converge when the fractional change in autocorrelation time (computed every 100 iterations) was one percent, and the number of iterations already computed was more than 100 times the autocorrelation time. The MCMC fit also was set to terminate if more than 10^5 iterations were run, but this only occurred for fits computed for asteroid encounters in which degeneracies were present, for example when the asteroid has rotational symmetry. About 10^4 iterations was often sufficient.

Before the MCMC was run, local minima in the likelihood were found via the Nelder-Mead algorithm implemented in `scipy` Gao & Han (2012). Generally, only one local minimum existed, except when $K_{22} = 0$ in which case rotational symmetry caused all values of γ_0 to be degenerate. Ensemble walkers were initialized near this local minimum, distributed by a Gaussian approximation of the likelihood, as determined via the Hessian of the likelihood at the minimum. Due to the high sensitivity of the angular velocity data to density moments, the minimization procedure sometimes failed to isolate the minimum likelihood. Therefore, a simpler simulation without the K_{3m} terms of equation 4 was first used to minimize likelihood as a function of the first-order parameters γ_0 and K_{2m} , and then the full simulation was used to find the second-order parameters K_{3m} with the first-order parameters fixed.

To further ensure convergence, we first minimized with respect to data truncated soon after perigee. After convergence, we refined the minimum by minimizing based on the full data, with the previous minimum as the initial estimate.

2.4 Density distribution constraints

The asteroid density distribution $\rho_A(r)$ is not uniquely constrained via tidal torque interactions because only the density moments $K_{\ell m}$ contribute to equation 4. For example, the

mass of the asteroid is unconstrained so $\rho_A(\mathbf{r})$ cannot be determined on an absolute scale. However, by making sufficient assumptions about the density distribution, we can nevertheless measure fluctuations in $\rho_A(\mathbf{r})$ across the asteroid from $K_{\ell m}$. To best understand the potential density distribution of an asteroid, an ensemble of models with differing assumptions is desired, so that common traits across the models can be identified. To this end, we thoroughly outline two possible models and discuss two more in appendix B.

We assume that the asteroid's surface is known in the inertial frame from radar data. Since the asteroid tumbles during the encounter, we also assume that the center of mass of the asteroid is extracted in the inertial frame. The density moments are extracted from flyby data, but these are known instead in the body-fixed frame.

To compare the asteroid surface and extracted density moments in the same coordinate system, we define a new frame called the “hybrid frame.” The hybrid frame is co-located with the body-fixed frame, but its orientation is known with respect to the inertial frame. (It has $\Omega_0 \parallel \hat{\mathbf{z}}_{\text{hybrid}}$ with third Euler angle $\gamma = 0$.) The hybrid frame differs from the body-fixed frame only by a rotation around $\hat{\mathbf{z}}_{\text{hybrid}} = \hat{\mathbf{z}}_{\text{body-fixed}}$ of γ_0 . Such rotations affect density moments via

$$K_{\ell m}^{\text{hybrid}} = e^{-im\gamma_0} K_{\ell m}^{\text{body-fixed}}. \quad (8)$$

by equation A9. Thus, values and uncertainties on $K_{\ell m}^{\text{body-fixed}}$ and γ_0 (obtained from the encounter data) can be translated into values and uncertainties on $K_{\ell m}^{\text{hybrid}}$. Henceforth, we will operate only in the hybrid frame and suppress the label.

When the K_{3m} are extracted, 15 moments are constrained (excluding K_{00}). Since the asteroid mass cannot be determined by this analysis, it is convenient to additionally set the mass equal to its volume, so that the average density is $\rho_{\text{avg}} = 1$ and thus the extracted densities can be interpreted as ratios of ρ/ρ_{avg} . Three of the moments are redundant with the center of mass, such that only twelve finite elements are free. In cases where γ_0 is known very accurately such that the uncertainty increase imposed by equation 8 is very small, it is numerically favourable to treat K_{2m} as fixed, just as $\Im K_{22}^{\text{body-fixed}}$ and $K_{21}^{\text{body-fixed}}$ are fixed. In this case, there are nine degrees of freedom (DOF). Since γ_0 is precisely known for all cases studied in this paper, we will always study this case. We also place additional constraints that $0.25 < \rho < 3$ to ensure realistic densities.

To extract a density distribution, we use another MCMC given one of the two parametrizations of density distributions discussed below. We also present two further models in appendix B which are viable substitutes for the following two models but are not used in the main text. The prior is set to be flat and non-zero for all configurations that obey the $0.25 < \rho < 3$ constraint. The likelihood used is set equal to the multivariate-Gaussian approximation of the posterior distribution for $K_{\ell m}$, extracted from flyby data.

2.4.1 Finite element model

To define the “finite element” model, we divide the asteroid into N finite elements of uniform density and use the density ρ_i of each as parameters. The four constraints imposed by the known mass and center of mass of the asteroid (seven with K_{21} and $\Im K_{22}$ are also fixed) are used to fix some of

the ρ_i . These constrained densities are easily computed since the asteroid mass μ_A and the product $I_A K_{\ell m}$ are both linear functions of ρ_i . Because $I_A K_{00} = a_A^2 \mu_A$ by definition (which is known), and $K_{\ell m} = 0$ implies that $I_A K_{\ell m} = 0$, $I_A K_{\ell m}$ is known for all the fixed moments, and computing the corresponding constrained densities is simply a matrix inversion.

The size and location of the elements must be chosen before extracting their densities. Best results generally require elements of equal size to be chosen. To remove the dependence on this choice, density distributions for many distinct element layouts can be extracted and the density of each point in the asteroid can be randomly sampled from any of these solutions to yield estimates for the mean density and uncertainty in density at each point.

The value of N must be carefully chosen, since it embodies a balance between the precision and accuracy of the resulting distribution. If N is set equal to the number of data points, an accurate solution is guaranteed, but uncertainties are inflated. If N is chosen lower, the choice of element layout might exclude a distribution that exactly matches $K_{\ell m}$, but uncertainties are diminished due to less redundancy in the model. For the rest of this paper, we use $N = 12$ finite elements, which corresponds to 7 constrained elements and 5 DOF.

To arrive at this choice of 5 DOF, we extracted five density distributions with uncertainties from five random grids for the asymmetric asteroid. We calculated the mean density uncertainty over the asteroid for all five grids σ_ρ , as well as the average deviation from the true density distribution $\Delta\rho$ and the significance of that deviation $\Delta\rho/\sigma_\rho$. We did this for different levels of observational precision and with either 9, 7, 5, 3, or 2 DOF. Our data revealed that 5 DOF appeared to show the lowest density uncertainty while still producing low significance of deviations from the true density distribution.

2.4.2 Lumpy model

A drawback of the finite element model is that the generated density distribution might not be representative of the asteroid if the elements are not optimally placed. We therefore describe an alternate model which includes the positions of the elements as parameters at the cost of resolution. We call this the “lumpy” model.

Suppose the asteroid is formed of N constant-density, possibly overlapping “lumps,” enclosed within a constant-density substrate whose surface is visible to observers. The substrate mass and added mass of the lumps are denoted by μ_i , each with position \mathbf{r}_i (relative to the asteroid's center of mass), density moments $K_{\ell m}^{(i)}$, and length a_i . Here, i denotes the index of the lump where the substrate is $i = 0$. We do not need to include I_i as a free parameter because these lumps have constant density, so that $I_i = \mu_i a_i^2$. Furthermore, by requiring that a lump's density moments be computed relative to the center of mass of the lump, we have $K_{1m}^{(i)} = 0$.

The translation rules of spherical harmonics van Gelderen (1998) give that the density moments in the hybrid frame are

$$K_{\ell m} = \left[\sum_{i=0}^N \frac{a_i^2 + r_i^2}{a_A^2} \mu_i \right]^{-1} \times \left[\sum_{i=0}^N \sum_{\ell' m'} \mu_i \frac{a_i^{\ell'}}{a_A^{\ell}} R_{\ell-\ell', m-m'}(\mathbf{r}_i) K_{\ell' m'}^{(i)} \right] \quad (9)$$

where the unmarked sum limits are $0 \leq l' \leq l$ and $-\ell' \leq m' \leq \ell'$. We also have total mass and center of mass constraints:

$$\mu_A = \sum_{i=0}^N \mu_i, \quad 0 = \sum_{i=0}^N \mu_i \mathbf{r}_i. \quad (10)$$

Additional constraints can be imposed on $K_{\ell m}^{(i)}$ if desired. For example, we can require that the lumps be ellipsoids, so that $K_{3m}^{(i)} = 0$. The most extreme case is that spherical lumps, which have $K_{\ell m} = 0$ for $\ell > 0$. $K_{00} = 1$ is also guaranteed by definition, meaning that each spherical lump has only five DOF (a_i , μ_i , and \mathbf{r}_i). The substrate has one degree of freedom, since only μ_0 is unknown. Thus, this spherical lumpy model has $5N - 3$ total DOF. Again, the choice of N affects the accuracy and uncertainty of the model results. For the rest of this paper, we use $N = 1$ lump for simplicity, corresponding to 2 DOF. In section 4.4, we also use $N = 2$ lumps which possesses 7 DOF.

3 RESULTS

To demonstrate our interior-probing methodology, we provide a full density distribution retrieval applied to synthetic data for two “reference asteroids,” which correspond to the following encounter parameter choices.

- (i) An orbit around a spherical, non-rotating, Moonless Earth with 6 km s^{-1} excess velocity and perigee at 5 Earth radii. This orbit was chosen to roughly match that of Apophis and corresponds to an eccentricity of 3.88.
- (ii) An initial roll of $\gamma_0 = \pi/8$.
- (iii) A cadence of 2 minutes and observational uncertainty of $\sigma_\theta = 10^{-2}$ and $\sigma_P/P = 10^{-7}$.
- (iv) A rotational period of 9 hours, with the angular velocity vector distributed between the $\hat{\mathbf{X}}$, $\hat{\mathbf{Y}}$, and $\hat{\mathbf{Z}}$ axes in a $1 : 2 : -2$ ratio.
- (v) An asteroid with radius $a_A = 1 \text{ km}$ and $K_{3m} = 0$. For K_{22} and K_{20} , we use two standard values: one with $(K_{22}, K_{20}) = (0, -0.097)$ and one with $(0.052, -0.202)$. Including the third point obtained by reflection $K_{22} \rightarrow -K_{22}$, these are the three points that minimize the mean distance between an arbitrary point in the allowed parameter space (equation A5) and these reference values. The first point is called the symmetric case because the corresponding uniform-density-ellipsoid model is rotationally symmetric around $\hat{\mathbf{z}}$. The second case and its reflection are called the asymmetric cases. Values of $(0.052, -0.202)$ have $a < b$ in the ellipsoid model, and the reflected value has $a > b$. If not specified, we use the $a < b$ case. Specifically, the asymmetric case has $a = 1140 \text{ m}$, $b = 1839 \text{ m}$, and $c = 565 \text{ m}$, while the symmetric case has $a = b = 1411 \text{ m}$ and $c = 1008 \text{ m}$.

In the following sections, we first introduce the retrieval capabilities regarding density moments, then we turn to the constraints that can be derived reliably on the density distribution. For both stages of information retrieval, we find that the results are consistent with the properties used to generate the synthetic data.

3.1 Density moment retrieval

Figure 2 shows our synthetic spin data for the asymmetric reference asteroid. The best-fitting model is overlaid in the

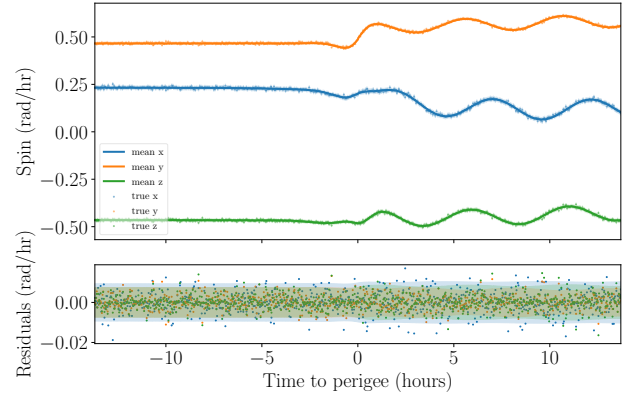


Figure 2. Data, best-fitting results, and residuals for a fit to synthetic data simulated for an asymmetric reference asteroid. Uncertainty bands are also shown. The best fit results are consistent with the data.

top panel and residuals are shown the bottom panel. Uncertainties are plotted on the residuals corresponding to the square root of the diagonal entries of the covariance matrix (correlations not included). The fit results are consistent with the data. This figure also reveals which data points are most informative. The at-perigee data is irregular and reveals information about the density moments, and the post-perigee data shows torque-free tumbling behaviour which constrains K_{2m} via the MOI ratios as in Moskovitz et al. (2020). The post-encounter periods and phase also indirectly sheds light on the at-perigee data by constraining the rotational velocity the asteroid must have had when leaving the perigee.

Figure 3 shows a corner plot of the PPDs of the ten parameters (namely γ_0 and $K_{\ell m}$ for $\ell \leq 3$), marginalized to functions of one (histograms) or two (contours) variables. The true parameters are shown and usually lie within 1 or 2σ of the $\Delta K_{\ell m} = 0$, where $\Delta K_{\ell m}$ is the difference between the posterior $K_{\ell m}$ and the true $K_{\ell m}$. The PPDs are generally Gaussian and sometimes show strong correlation between parameters, but no continuous degeneracy occurs. We performed 48 independent minimizations of the likelihood before the MCMC fit began, each with an initial point chosen randomly in the parameter space. All converged to the same minimum, demonstrating that the model lacks discrete degeneracy as well.

3.2 Density distribution retrieval

Figure 4 displays density distributions extracted by both the finite element and lumpy models for the reference asteroids. For the finite element model, five DOF and 20 different element layouts were used. The figure demonstrates that the finite element model successfully extracts density distributions consistent with the input density moments, as shown by the χ^2 value per degree of freedom, χ_r^2 , depicted in the figure. These express the agreement of the density moments of the shown distributions with the posterior distributions for the density moments, produced by the MCMC described in section 2.3. $\chi_r^2 = 0$ indicates that the moments of the shown distributions are exactly equal to the means of the moment posterior extracted by the MCMC. The accuracy of this model is robust for other shapes, including non-ellipsoidal shapes.

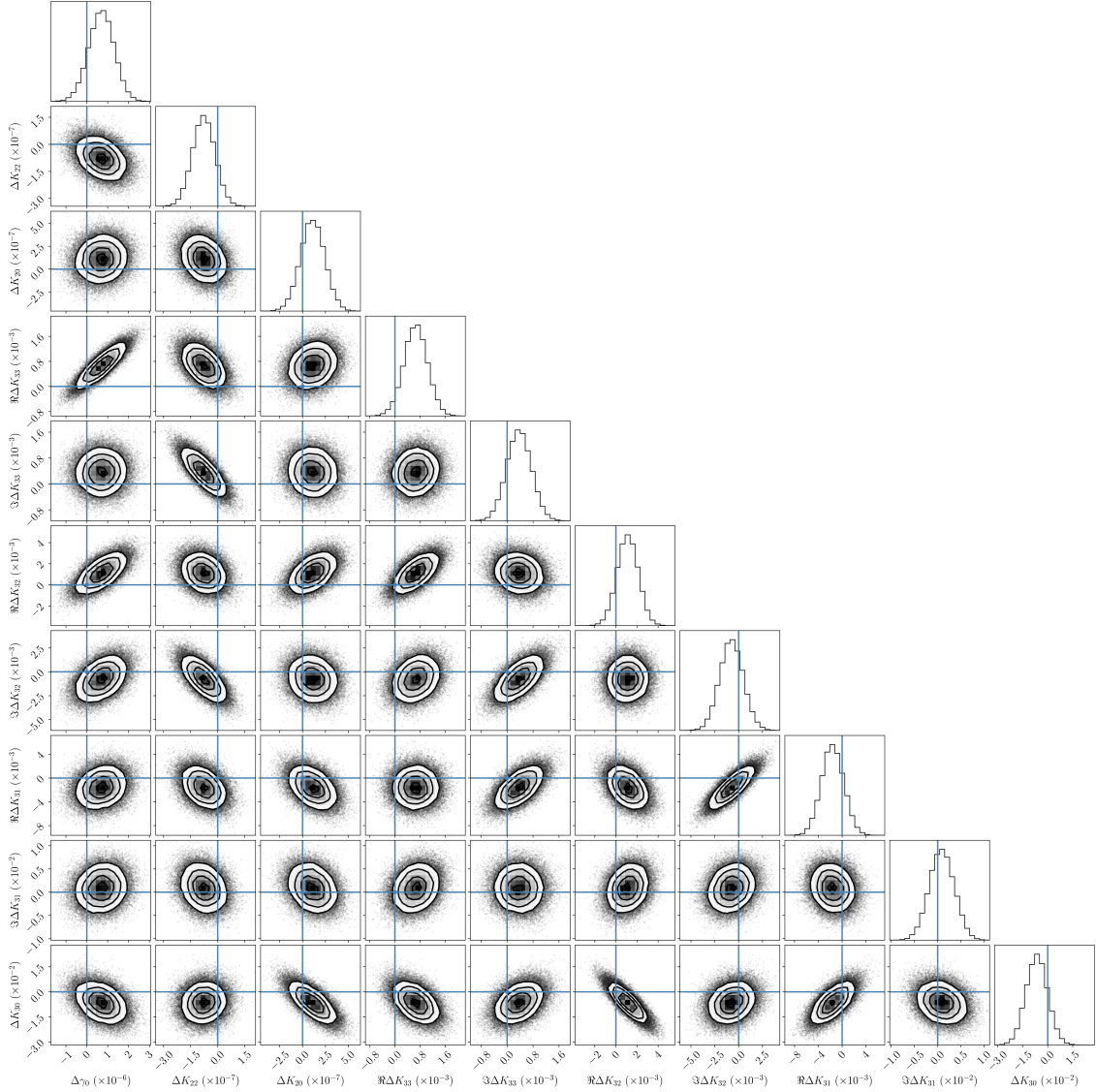


Figure 3. PPDs extracted from synthetic encounter data for the asymmetric reference asteroid. Samples from the MCMC fit are shown as individual points, and the contours enclose 1, 2, and 3σ confidence regions. True values are shown as blue lines. PPDs are Gaussian and show no degeneracies.

Furthermore, the finite element density distributions are consistent with uniform, which is the true density distribution of the asteroid. For the reference asteroid observational set-up, the uncertainty on observations is such that the density distribution is generally within 10% of the true density (second column) while the density uncertainty is generally less than 40–50% of the density value at any point in the asteroid (third column). The dependence of this constraint on the observational set-up is discussed in section 4.1. In no place is the significance of these deviations from the true distribution greater than 1σ (last column).

The lumpy model also yields distributions which are consistent with the extracted moments and consistent with uniform. These distributions have much lower uncertainty than the finite element distributions (maximum uncertainty on the order of 1% of the local density or less) due to its few degrees of freedom. With the one-lump-model and with aster-

oids whose surface’s centroid is the asteroid’s center of mass (such as these uniform asteroids), the single lump must lie at the centroid with mass close to zero and unconstrained radius. The uncertainty of regions far from the asteroid center, where the lump is unlikely to extend, is typically very small, while regions close to the center are more likely to be contained inside a lump and hence have greater density uncertainty.

We also explore model behaviour in non-uniform density asteroids. We employ an asteroid of the same shape as the asymmetric asteroid, and in the same flyby scenario, but we place a solid core of radius 300 m and density 50% greater than the surrounding density, 500 m away from the center of the asteroid. This changes the asteroid density moments. New density moments are extracted via the process described in section 2.3 and the finite-element and lumpy models are used to extract density distributions shown in figure 5.

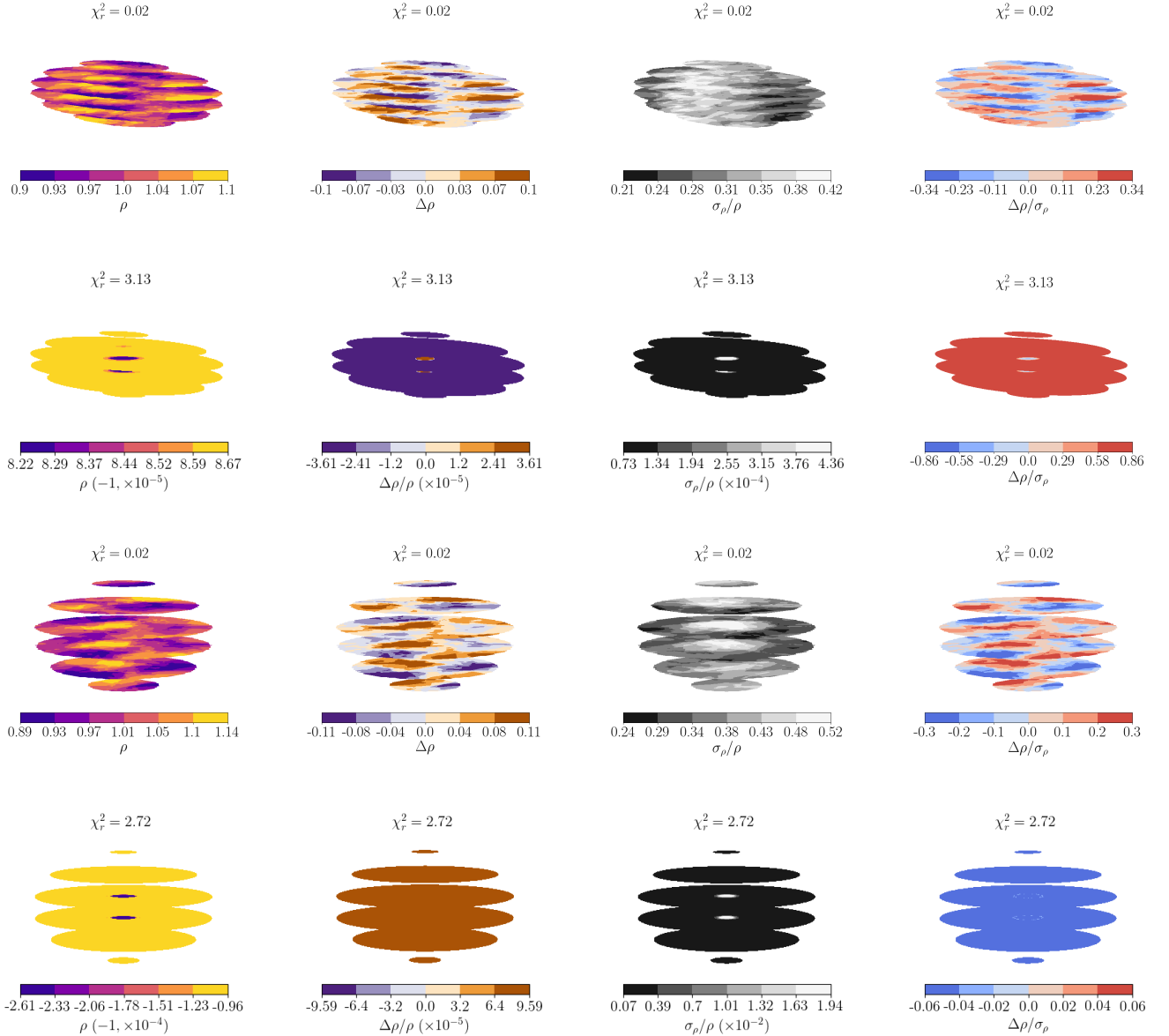


Figure 4. Cross-sectional slices of the density distributions extracted via the finite element model for the asymmetric (top two rows) and symmetric (bottom two rows) uniform-density reference asteroids. The finite element model (first and third rows) and the lumpy model (second and fourth rows) are employed. From left to right, the densities (divided by the average density), deviations from the true density, uncertainties, and significance of the deviations are plotted. These figures are available in animated form in appendix figure D1. Extracted densities are generally within 10% of the truth.

Once again, figure 5 shows that the model results are successful in that they reproduce the extracted density moments (χ_r^2 is low). However, the density distributions extracted by the finite model matches the true distributions less well. The deviation from the true density extends to as much as 17% in some locations, leading to a maximum significance of 0.52σ . Uncertainties are large enough that the distributions are consistent with the true distribution, but the finite element model has distributed the core into the rest of the asteroid so that the peak density is lowered.

On the other hand, the lumpy model is designed to detect discrete changes in density distribution, and identifies the boundary of the core very accurately. Deviations from the

truth are around 10^{-5} of the local density, with uncertainties about 1% of the local density at maximum and usually much lower. The significance of the deviations is around 30%, as it was in figure 4 where the extracted distribution again matched the truth. Again, the low uncertainty is caused by the small number of degrees of freedom of the lumpy model. A consequence is that if the core had been non-spherical, the lumpy model would be inaccurate, with significant deviations from the truth. Therefore, neither model is more correct in the general case, but each can be used to explore different scenarios.

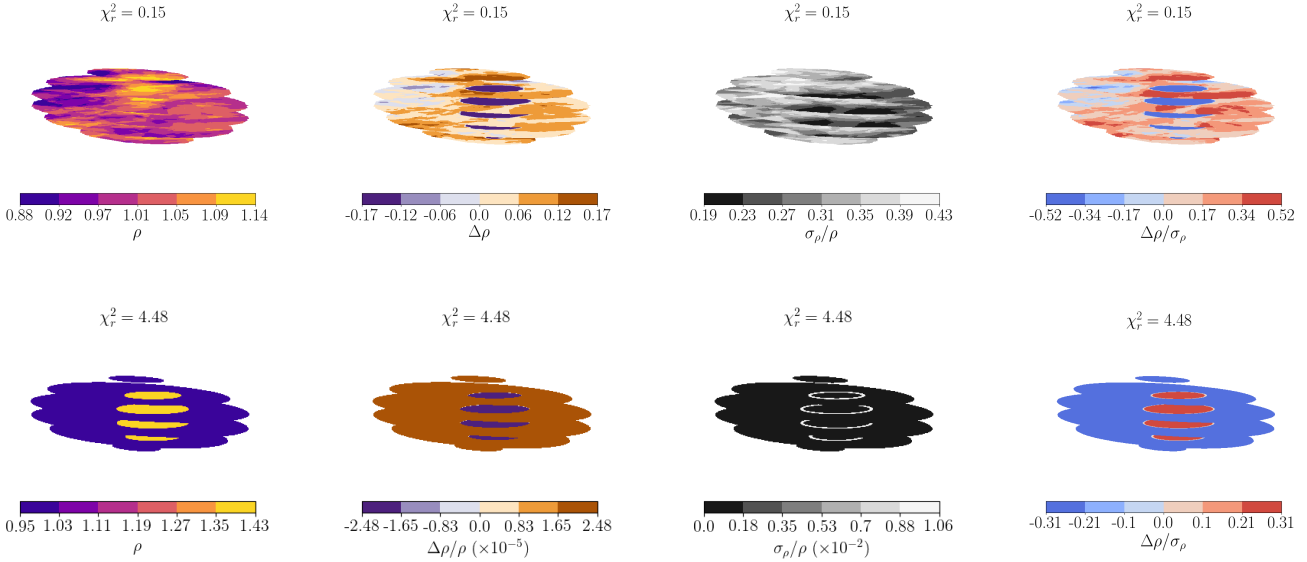


Figure 5. Cross-sectional slices of the density distributions extracted via the finite-element (*top*) and lumpy (*bottom*) models for an asteroid with an off-center core. From left to right, the densities, deviations from the true density, uncertainties, and significance of the deviations are plotted. These figures are available in animated form in appendix figure D2. The lumpy model successfully extracts the core.

4 DISCUSSION

4.1 Dependence of uncertainty on encounter properties

The question of which encounters are most suited to this methodology is of great interest, as is the question of how observational campaigns can be designed to best take advantage of an asteroid and maximize the success of this methodology. We investigate physical asteroid properties (the encounter’s orbital properties, the asteroid’s true shape, and its initial rotational velocity) and observational parameters (the data uncertainty, the cadence of observations, and gaps in data coverage), and discuss their effect on the uncertainty of this methodology’s results.

We study both the uncertainties on the density moments and uncertainty on density distribution. Moment uncertainty $\sigma(K_{\ell m})$ is defined as the range of $K_{\ell m}$ values that contains 68.27% of the marginal PPD for each ℓ and m . Since there is no degeneracy between moments and the actual encounter data, this uncertainty is well-defined. However, its physical relevance is not obvious. The density distribution uncertainty σ_ρ/ρ is defined as a map of uncertainty over the asteroid, made by taking the standard deviation of density at each point over 5000 maps of asteroid density, each corresponding to a random sample of the output of the density distribution MCMC described in section 2.4. The median of this uncertainty divided by the local density over this map is taken to represent the density distribution uncertainty. This measure of uncertainty is more physically relevant than moment uncertainty, but it is strongly dependent by choices of the density distribution model, degrees of freedom, prior constraints, and other effects unrelated to the encounter properties. We therefore investigate both measures of uncertainty.

Table 1 displays the encounter properties corresponding to density distribution uncertainty equal to two sample values

Encounter property	Weak	Strong
Perigee (r_p , Earth radii)	<6.0	<18
Excess velocity (v_∞)	-	-
Asteroid length (a_A , m)	>15	-
Period (P_ω , hr)	>7.6	-
Spin period uncertainty (σ_P , ms)	<12	<270
Spin pole uncertainty (σ_θ , °)	<1.9	<35
Cadence (Δt , min)	<15	-
Data gap (T_{gap} , hr)	-	-

Table 1. The weak and strong thresholds on physical / observational properties (*top* / *bottom*) consistent with useable density distribution uncertainty. Perigee and observational uncertainty are the most constraining properties, followed by rotational period, asteroid length, and observational cadence.

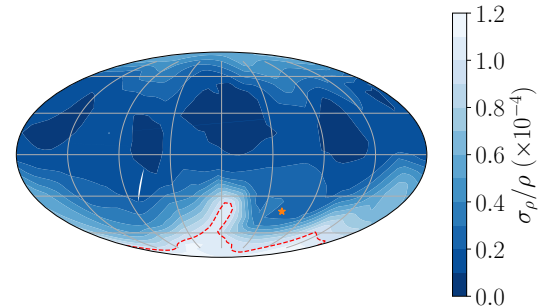


Figure 6. Median ratio of density uncertainty to density computed over the reference asteroid density distribution via the lumpy model as a function of initial spin pole direction. The weak uncertainty cut-off (red line) is shown, as is the reference spin pole direction (orange star). The strong cut-off is never exceeded and thus does not appear. Initial angular velocities perpendicular to the orbital plane lead to greatest uncertainty.

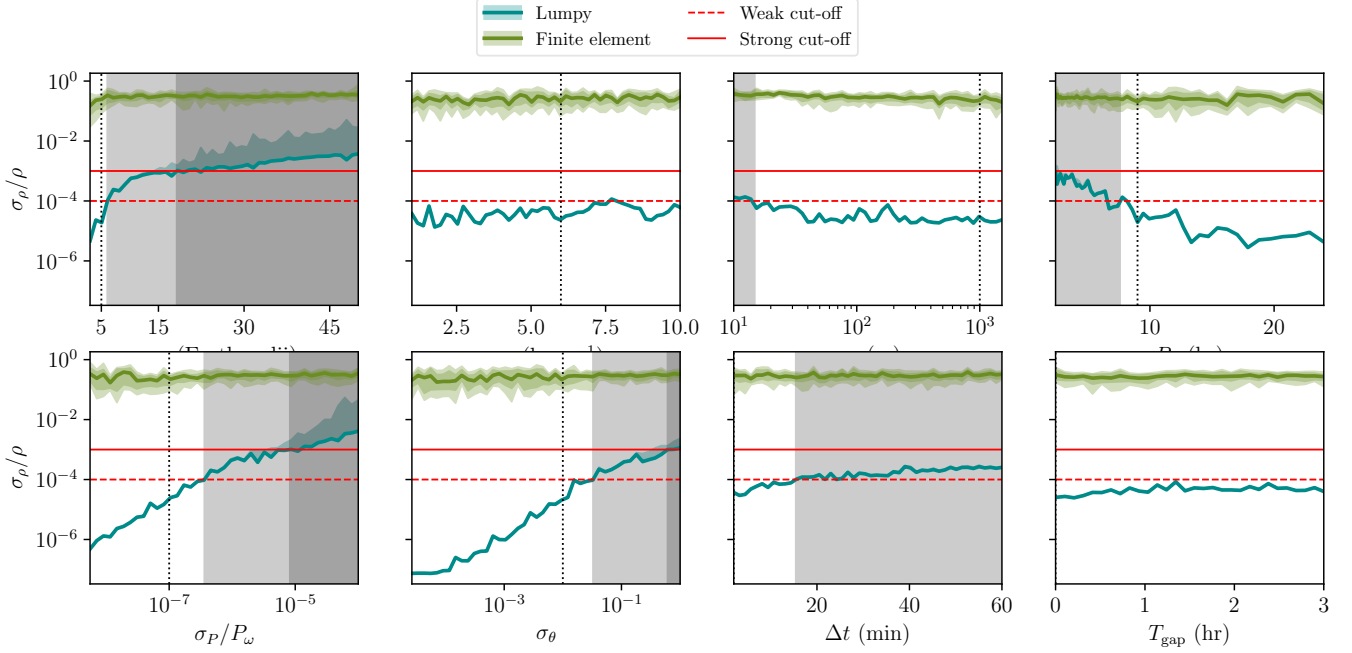


Figure 7. Median ratio of density uncertainty to density computed over the reference asteroid density distribution as a function of physical / observational encounter properties (*top / bottom*). Density distributions from both the lumpy and finite element models are used. The uncertainty thresholds (red lines) are shown and the properties that exceed these thresholds are shaded. The vertical black dotted lines are the property values of the reference asteroid. The figures illustrate the marked difference in density distributions that results from using different models.

we term the “weak” and “strong” thresholds. These values are $\sigma_\rho/\rho = 10^{-4}$ (weak) and 10^{-3} (strong), for density distributions extracted via the lumpy model. They are manually chosen, and adjustments to them or to the lumpy model will affect the data of table 1. Figure 6 depicts the same σ_ρ/ρ as a function of initial spin pole direction, while figure 7 depicts σ_ρ/ρ as a function of the encounter properties. Both highlight the threshold values of table 1 with red lines. Bands containing 68% (light) and 95% (dark) of the density uncertainty over the asteroid are shown for figure 7.

Table 1 reveals that the most limiting physical properties of the asteroid are its perigee and period. Excess velocity does not greatly affect the uncertainty of the density distribution, and asteroid length is only effective for $a_A \sim 15$ m. By contrast, the radius of Apophis is ~ 300 m and its perigee and rotational period also obey the strong constraints Giorgini et al. (2008). The comparison to Apophis is complicated by the fact that Apophis is smaller than our a_A value, is tumbling Pravec et al. (2014), and may change slightly in physical properties due to tidal interaction during the encounter Yu et al. (2014); Hirabayashi et al. (2021). Further work must therefore be done to apply this analysis to Apophis.

In addition to the period constraint shown in this table, figure 6 shows a threshold on initial spin pole direction. The poles (i.e., angular velocities perpendicular to the orbital plane) lead to greater uncertainty and this is the only region which rises above the weak uncertainty threshold.

Table 1 also demonstrates the strong effect of properties of the observational campaign on the final density uncertainty. Most vital are the uncertainty on the instantaneous asteroid rotational period σ_P/P and its direction σ_θ , which require precision on the order of tens to hundreds of milliseconds

and degrees every cadence, respectively. This could be accomplished by multiple, precise angular velocity measurements from multiple telescopes, or by increasing the time between observations to maximize the change in period between observations. Acknowledging and correcting for correlations in uncertainty between data points could also reduce uncertainty. Increasing the data set size to include more post-flyby tumbling data would also increase precision on some parameters, especially K_{2m} , without requiring such high period uncertainty.

On the other hand, the cadence of observations Δt and the presence of gaps in the data T_{gap} do not affect results as strongly. Observations can be as much as 15 minutes apart to obey the weak threshold, with no constraint required to meet the strong threshold in our data set (which contains $\Delta t < 1$ hr). Likewise, there is no constraint on our data set of $T_{\text{gap}} < 3$ hr. This gap was simulated to occur in one contiguous unit centred on the encounter perigee, where torque is highest. If the gap occurred elsewhere in the data set or was subdivided into multiple gaps, it would likely affect density uncertainty even less. All of these thresholds are liable to change if the encounter properties are adjusted, since they are all interdependent.

Figure 7 reveals that the thresholds presented in table 1 are particularly sharp (a steep slope of σ_ρ/ρ) for the encounter perigee r_p and observational precision σ_P and σ_θ . These thresholds are therefore less likely to change if the asteroid properties are altered, whereas the thresholds on period P_ω , length a_A , and cadence Δt are more volatile. The figure also displays the stark difference between density uncertainty computed by the lumpy model and the finite element model. This is partially due to different choices in the

number of DOF (5 for the finite element model and 2 for the lumpy model), and to the assumptions of the model; the lumpy model is more biased towards uniform asteroids such as these, since it is comprised of a small number of uniform density regions. This model-dependence of σ_ρ/ρ is another reason to take the thresholds of table 1 as estimates rather than strict limits on encounter properties.

To address the dependence of σ_ρ/ρ on the choice of model, we investigate the model-independent moment uncertainty as well. Figures 8 and 9 display moment uncertainty $\sigma(K_{\ell m})$ as a function of physical and observational encounter properties respectively. Figure 10 additionally depicts moment uncertainty as a function of initial spin pole. The thresholds of table 1 are depicted as red lines.

Figure 8 reveals that σ_ρ/ρ is more sensitive to $\sigma(K_{2m})$ than to $\sigma(K_{3m})$. For instance, $\sigma(K_{2m})$ is constant as a_A is varied despite a dramatic increase in $\sigma(K_{3m})$ for low a_A . The resulting σ_ρ/ρ is mostly constant. The opposite is true for P_ω , where $\sigma(K_{3m})$ (except for $m=0$) are mostly constant, and σ_ρ/ρ follows the trend of $\sigma(K_{2m})$ and increases for low rotational period. A consequence is that if more post-flyby tumbling data is collected, placing stronger constraints on K_{2m} rather than K_{3m} , then K_{2m} at some point might have essentially no uncertainty. In this case, uncertainty on K_{3m} will be dominant and the most constraining parameters will change. Rotational period P_ω will cease to be a vital parameter but asteroid length a_A will be because $\sigma(K_{3m})$ are much more dependent on a_A than P_ω .

In the following sections, we study each panel of figures 8 and 9 individually and discuss their implications.

4.1.1 Orbital elements

A Keplerian orbit is completely described by five parameters, but three describe the orbit's orientation with respect to the central body. They are therefore redundant with the orientation of the inertial frame and we do not investigate them here. We parametrize the remaining two parameters by the perigee distance r_p and excess velocity v_∞ .

Figure 8 shows a very strong dependence on perigee as mentioned in the main text — so strong that for large perigee, $\sigma(K_{3m})$ is constrained by the prior boundaries of ± 1 for $m < 3$. This occurs as low as $r_p = 10$ Earth radii for K_{30} , though the fact that density distributions can still be extracted at this perigee value shows that resolution of K_{30} is not essential to extract density distributions. Figure 7 also demonstrates that low perigee yield more certain density distributions as extracted by both the lumpy and the finite element models. Such a strong dependence is expected from equation 4; it is caused by the $(a_A/D)^\ell$ dependence of the tidal torque on distance D .

By contrast, density moment uncertainty shows only a slight increase with v_∞ . This is likely due to the fact that larger v_∞ leads to a faster and flatter orbit with less time spent close to the planet, where tidal torque is strongest. This change in encounter timing also adjusts the orientation of the asteroid at perigee, which has a separate effect on moment uncertainty. We control for this undesired orientation dependence by adjusting γ_0 so that, if no tidal torque is present, the orientation of the asteroid at perigee is constant for all v_∞ . The effect of tidal torque then causes orientations to be

roughly the same at perigee where tidal torque is highest. This effectively removes the orientation dependence.

4.1.2 Rotational period

In figure 8, we show $\sigma(K_{\ell m})$ as a function of rotational period P_ω . As in the above section, the value of γ_0 was corrected to ensure roughly constant orientation at perigee. K_{20} and K_{22} show very large uncertainty for $P_\omega \lesssim 4$ hr because these fast rotators tumble very little after perigee. This increases uncertainty on the K_{2m} parameters, which are largely constrained by post-encounter tumbling.

We expect that fast rotators would not tumble post-encounter because, for small P_ω , all the dynamical variables vary much more slowly than the orientation γ . Approximating each variable as constant over one full rotation of γ , the integral of the first-order contribution of τ over $\gamma \in (0, 2\pi)$ gives no secular first-order torque to force the asteroid to tumble. However, this effect does not apply to the second-order parameters, since the integral over the second-order term of τ does not vanish, as seen in the figure. An asteroid with large K_{3m} moments might therefore be yield better uncertainties at these low rotational periods (e.g., a non-uniform or non-elliptical asteroid).

Another feature of figure 8 is that $K_{\ell 0}$ is more uncertain at low P_ω than the other parameters (most visible for K_{30}). The explanation is likely the following: Tidal torque components τ_x and τ_y induce tumbling, and since fast rotators exhibit reduced tumbling post-encounter, these components likely have little effect on moment uncertainty. The most observable component of torque is then τ_z , but equation 4 shows that $K_{\ell 0}$ does not contribute to τ_z . Asymmetry is therefore more measurable than symmetry for these fast rotators.

4.1.3 Initial spin pole

The tidal torque experienced by the asteroid is affected by the initial direction of asteroid spin Ω_0 both because spin sets the initial asteroid orientation up to γ_0 and because of the spin-dependence of the rotational equations of motion (equation A14).

Figure 10 depicts increased moment uncertainty for initial spin pole $\Omega_0 \parallel \hat{Z}$, just as 6 depicts increased density distribution uncertainty. Many other moments also exhibit increased uncertainty for $\Omega_0 \parallel \pm \hat{Y}$. This pattern is explained by the tidal torque equation (equation 4). By plugging in values for the Euler angles, $z \parallel \hat{Z}$ and $z \parallel \hat{Y}$ at perigee lead to $\tau \propto K_{22}\hat{z}$ to first-order, and $\tau \parallel \hat{X}$ at perigee leads to $\tau = 0$ to first-order. $\tau \parallel \hat{z}$ implies that only the period of the asteroid is changed, not its spin pole direction. In the case of $\Omega_0 \parallel \hat{Z}$, we therefore expect $\Omega \parallel \hat{Z}$ throughout the encounter so that the asteroid does not tumble after the flyby. As discussed in the main text, tumbling allows precise constraints on K_{2m} , so that reduced tumbling results in greater uncertainty.

We may understand the case of $\Omega_0 \parallel \hat{Y}$ by the approximation that τ is small until perigee, so that the direction of Ω is unchanged. Insofar as this assumption is accurate, the behaviour of $\Omega_0 \parallel \hat{Y}$ will be similar to that of $\Omega_0 \parallel \hat{Z}$, explaining the increased moment uncertainty in this region. This argument breaks down for $\Omega_0 \parallel \hat{X}$, because here $\tau = 0$,

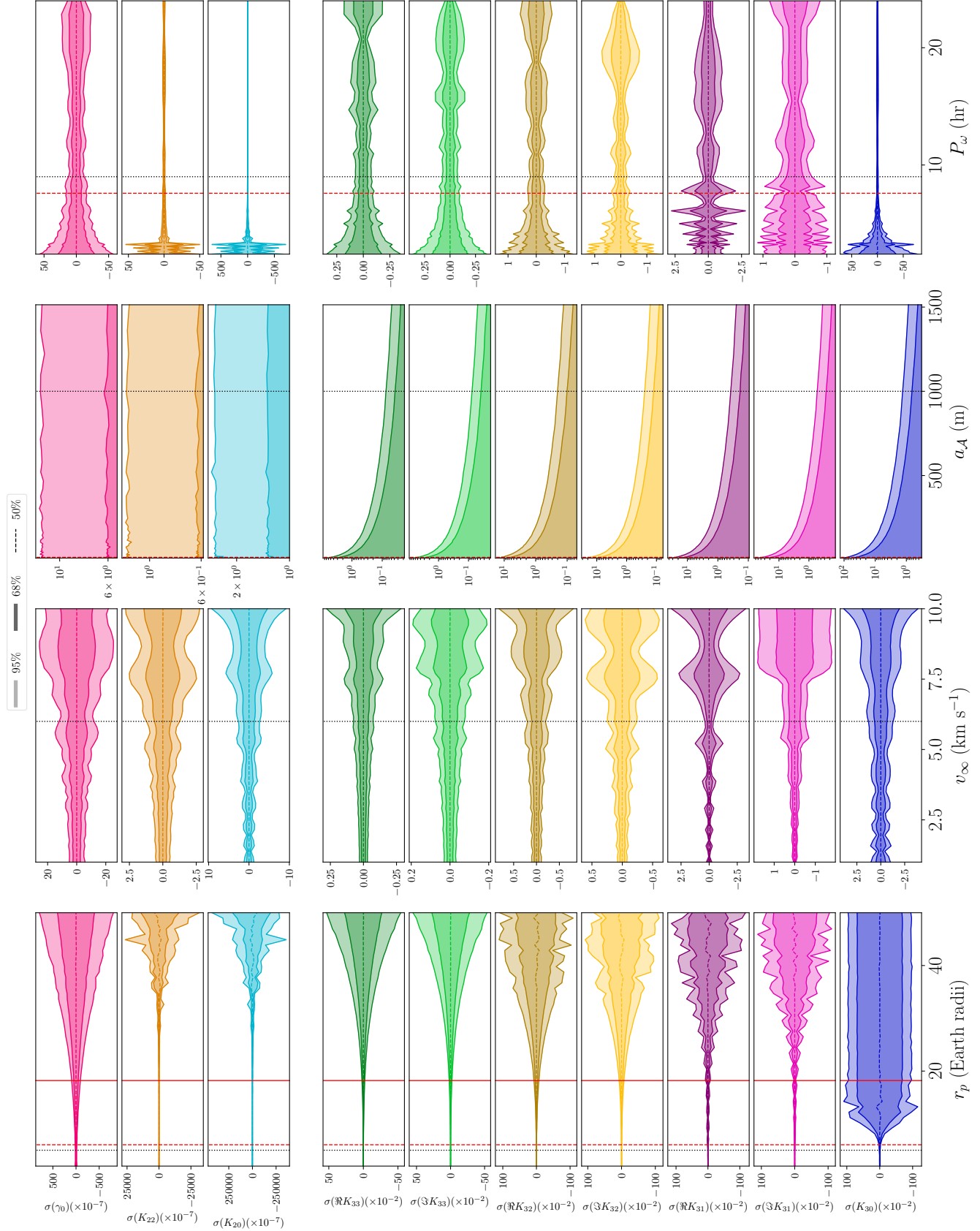


Figure 8. 1 and 2σ confidence intervals for the first-order parameter PPDs (top) and second-order parameters (bottom) as a function of (left to right) perigee, excess velocity, asteroid length, and rotational period. The vertical dotted line indicates the reference asteroid values. The red solid/dashed lines indicate the weak/strong uncertainty thresholds.

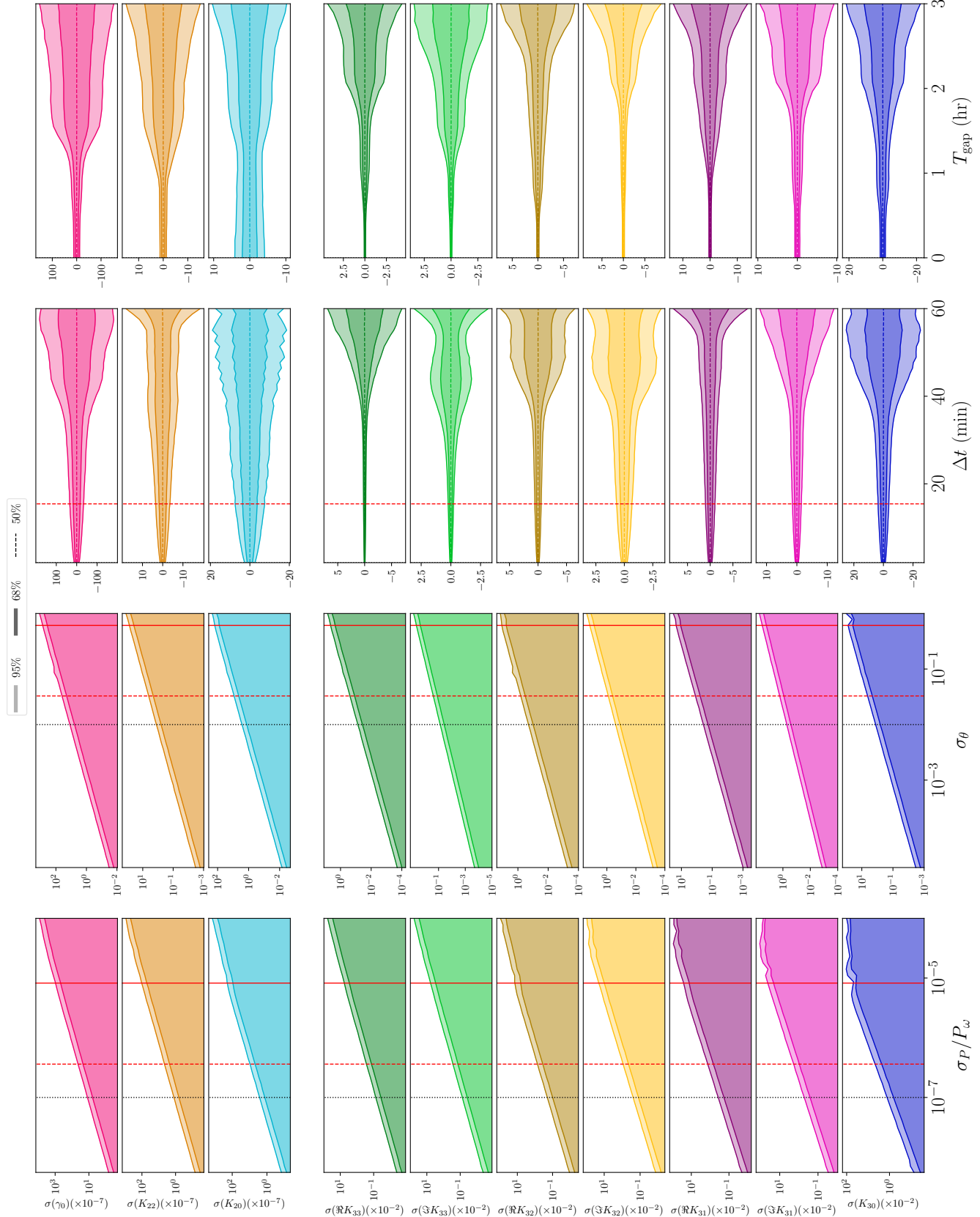


Figure 9. 1 and 2 σ confidence intervals for the first-order parameter PPDs (*top*) and second-order parameters (*bottom*) as a function of (left to right) period and spin pole uncertainty, observational cadence, and length of gaps in the data. The vertical dotted line indicates the reference asteroid values. The red solid/dashed lines indicate the weak/strong uncertainty thresholds.

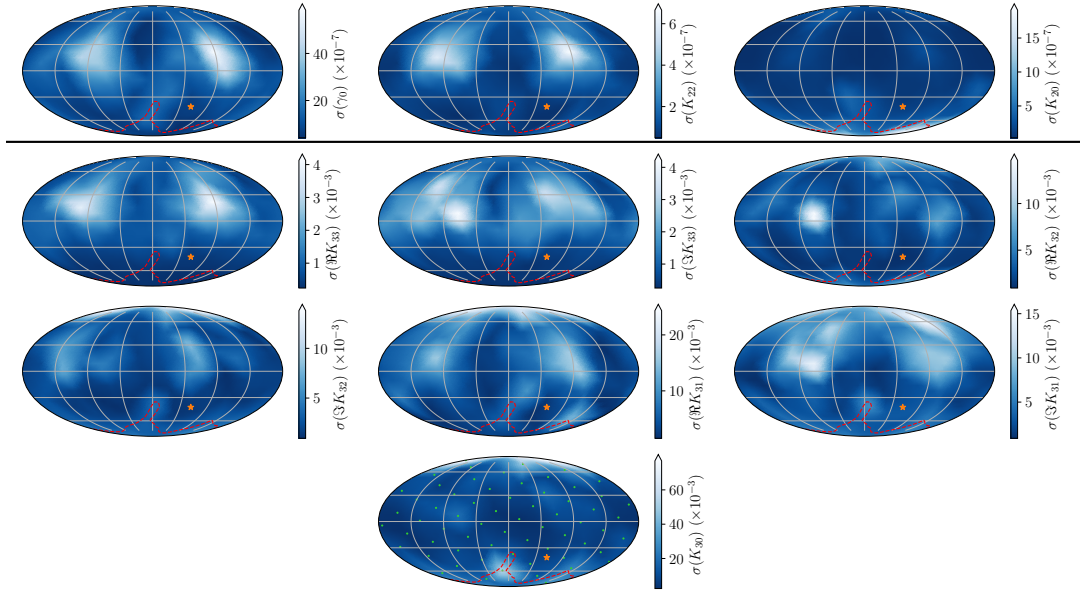


Figure 10. 1σ uncertainties for the first-order parameters (*top*) and second-order (*bottom*) as a function of the initial direction of spin in the inertial frame. All maps are made in the Mollweide projection. The orange star indicates the reference spin pole. Green dots are the sampled spin pole directions. The red contours enclose regions above the strong uncertainty threshold on σ_ρ/ρ . The weak threshold is never exceeded. Beyond the $\pm \hat{\mathbf{Z}}$ increase in uncertainty, there is also increased moment uncertainty for $\pm \hat{\mathbf{Y}}$.

and torque is dominated by non-perigee effects. This may explain why there is no increased uncertainty near $\Omega \parallel \hat{\mathbf{X}}$.

4.1.4 Observational uncertainty

Two parameters, σ_θ and σ_P , govern the observational uncertainty of the data set. These parameters are defined in section 2.2; σ_θ represents the standard deviation of the angle between the true spin pole and the observed spin pole, while σ_P represents the standard deviation of the rotational period. Rather than explore the full space spanned by these two values, we fix one and allow the other to vary to better assess whether uncertainty in spin pole or uncertainty in period more strongly affects uncertainty. This dependence is displayed in figure 9. Moment uncertainty ($\sigma(K_{\ell m})$) grows linearly with observational uncertainty (σ_θ or σ_P).

In particular, we might ask if some error δ_ω is added to angular velocity ω , does it affect results more strongly if it is parallel to ω (affects the period) or perpendicular (affects the spin pole direction)?

Let $\delta = |\delta_\omega|/|\omega|$ and $\delta \ll 1$. Then if $\delta_\omega \parallel \omega$, it decreases the period P_ω by $P_\omega \delta$. This is a fractional change in period of δ . If $\delta_\omega \perp \omega$, then the spin pole angle changes by δ radians. Comparing the σ_P/P (fractional change in period) and σ_θ (spin pole angle) columns of figure 9, one can see that a given value of σ_θ contributes a much smaller moment uncertainty than the same value of σ_P/P . This is also visible in figure 7 for the lumpy model. In other words, if $\delta_\omega \perp \omega$ using the symbols defined above, then $|\delta_\omega|$ can be large. But if $\delta_\omega \parallel \omega$, then $|\delta_\omega|$ must be very small. Period precision is therefore more vital than spin pole direction precision when it comes to decreasing uncertainties.

4.1.5 Cadence

The time between observations of asteroid angular velocity, (cadence, Δt), may vary depending on the observational schedule of the observing telescopes and the path of the asteroid through the sky. We measure how the moment uncertainty $\sigma(K_{\ell m})$ varies with cadence ranging from two minutes to one hour in figure 9.

Figure 9 displays little dependence of uncertainty on cadence Δt for $\Delta t \lesssim 40$ min. We also see flaring of uncertainty for very large cadence, largely driven by the paucity of data points. However, uncertainty dramatically increases for many parameters at about $\Delta t = 30 - 40$ min, a time scale which depends both on the asteroid rotational period P_ω and the time scales of its orbit.

Figure 9 shows that as long as Δt is less than this threshold, the influence of cadence on σ is small, but shorter cadence leads to lower uncertainties.

4.1.6 Data gaps

In certain circumstances, spin data might not be able to be captured for a close encounter at perigee. The asteroid might dip below the horizon, or it might pass too close to the sun to be observed. The resulting gap in data is intended to be captured by the T_{gap} parameter of figure 9, which deserves to be more fully defined.

We mask the perigee of the counter by removing a duration T_{gap} of data centred on the perigee, where T_{gap} ranges from 0 to 3 hours. To prevent lack of precision induced by lower amounts of data when T_{gap} is large, we always cut 3 hr $- T_{\text{gap}}$ from the data set, half from the beginning and half from the end, so that each data set produced for all T_{gap} has the same size. We cut around the perigee because tidal torque is the greatest at perigee, and we expect that part of

the data set to be most valuable. Indeed, figure 9 shows that K_{3m} especially are more uncertain for $T_{\text{gap}} \gtrsim 1.5$ hr. However, figure 7 shows that T_{gap} never increases density uncertainty above the thresholds, indicating that large amounts of data can be cut without compromising the methodology. As with the threshold for cadence discussed above, this 1.5 hr cut-off may depend on the asteroid rotational period or the orbital time scales. It likely also depends on the observational cadence used.

4.1.7 Other parameters

We also study the dependence of moment uncertainty on the asteroid MOI and on the asteroid's initial orientation, but these relationships are simple enough that they are not included in figures 8 and 9. Moment uncertainty is generally unrelated to the asteroid shape, except when the asteroid is rotationally symmetric (e.g., for the symmetric reference asteroid). In this case the initial orientation of the asteroid γ_0 is undefined, creating degeneracy and inflating density moment uncertainty. For symmetric or near-symmetric asteroids, this issue could be resolved by re-parametrizing the MCMC to remove this degeneracy.

Moment uncertainty is also affected by γ_0 , which was corrected for in section 4.1.1. We measured the moment uncertainty as a function of γ_0 for the asymmetric reference asteroid, keeping all other parameters constant. Moment uncertainties varied by factors of **JTD: 25-100%**, generally exhibiting roughly sinusoidal behaviour. The details of this dependence are strongly dependent on the initial spin pole and the asteroid shape.

4.2 Central body oblateness

In all the above studies, we assumed a spherical planet ($J_{\ell m} = 0$ for $\ell \geq 1$). $J_{1m} = 0$ is enforced by the coordinate definitions, so the effect of central body non-sphericity is limited to the J_{2m} terms and damped by a factor of $(a_B/D)^2$. We expect these parameters to have small effect on the asteroid behaviour.

Here, we define oblateness as $\epsilon = (I_z - I_x)/(\mu_B R_B^2)$, where $I_{x,y,z}$ are the central body moments of inertia along the principal axes, and $I_x = I_y$. R_B is the true radius of the body (not a_B from equation 3). For an equatorial orbit, ϵ and the central body density moments (equation A3) are related by $J_{\ell m}$ as $\epsilon = -10J_{20}/3$ and $J_{22} = 0$. Since an oblate ellipsoid is mirror-symmetric around all three axes, J_{3m} are all zero. The next order of tidal torque is therefore J_{4m} , damped by an additional $(a_B/D)^2$ factor, and non-ellipsoid corrections to the central body shape. We do not consider these extra factors.

Figure 11 displays moment uncertainty $\sigma(K_{2m})$ of the first-order parameters as a function of ϵ across a reasonable range of central body oblatenesses based on those of Solar System planets Pater & Lissauer (2015). It also shows linear best-fitting curves for moment uncertainty as a function of oblateness. All other parameters, include I_B which parametrizes the central body radius, are kept constant. Almost no dependence of $\sigma(K_{\ell m})$ on oblateness ϵ is apparent, although moment uncertainty does measurably decrease for oblate central bodies.

Given the small effect of ϵ on $K_{\ell m}$, it might be tempting to

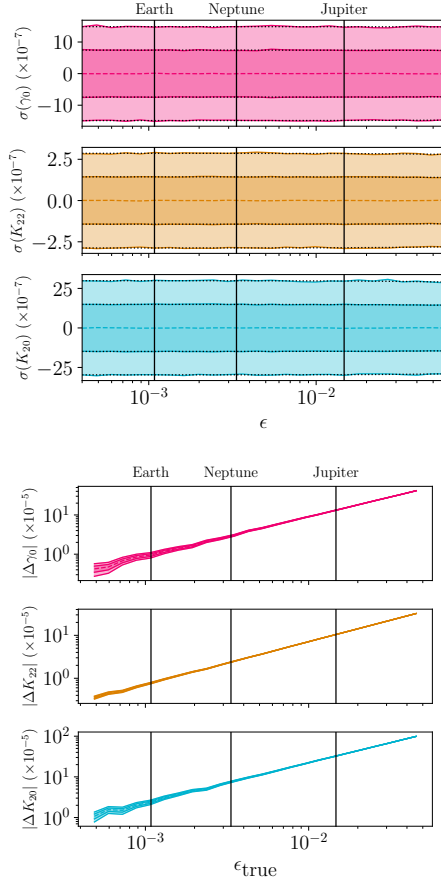


Figure 11. Top: 1 and 2 σ confidence intervals for the first-order parameter PPDs as a function of oblateness ϵ . All other parameters, including the central body radius, are kept constant. Linear best-fitting lines to $\sigma(K_{2m})$ (black, dotted) are plotted. Bottom: The difference between PPD means extracted from a zero-oblateness model and the true parameters given data with true oblateness $\epsilon_{\text{true}} \neq 0$. Also shown in both figures are the oblatenesses of reference Solar System bodies. Moment uncertainty depends little on oblateness, but the best-fitting parameter estimates are affected enough by oblateness that oblateness must still be modelled.

neglect the planetary oblateness when fitting $K_{\ell m}$ to data. However, the bottom panel of figure 11 demonstrates that doing so is invalid. This figure displays $K_{\ell m}$ as extracted by a fit assuming $\epsilon = 0$, but run on data generated with non-zero ϵ . The difference between the PPD means and true parameters are shown. Moment uncertainties are also shown as bands. The figure shows that even for low (Earth-scale) oblateness, the fit results are inconsistent with the true $K_{\ell m}$ values, since $\Delta K_{\ell m} = 0$ is not contained in the 2 σ band. This effect is much worse for large oblateness, growing to a difference on the order of $\mathcal{O}(100)\sigma$ for Jupiter's oblateness. Therefore, accurately modelling central body oblateness to high precision is essential for the accurate estimation of fit parameters. For non-equatorial orbits, with $J_{22} \neq 0$, we also expect J_{22} to affect the accuracy of the fit results to a similar degree, with the additional requirement of using the correct asteroid orbital plane.

J_{20} has a slightly more general definition than oblateness. If the planet has a moon, the integral defining J_{20} (equation

$K_{\ell m}$	$\sigma(K_{\ell m})_{\text{Jupiter}}/\sigma(K_{\ell m})_{\text{Earth}}$
γ_0	1.6
K_{22}	2.3
K_{20}	11
$\Re K_{33}$	18
$\Im K_{33}$	18
$\Re K_{32}$	18
$\Im K_{32}$	18
$\Re K_{31}$	25
$\Im K_{31}$	10
K_{30}	53

Table 2. Ratio of moment uncertainty for all density moments $K_{\ell m}$ between an Earth encounter and a Jupiter encounter with identical properties except for an increased perigee. Observational uncertainty and cadence are assumed to be equivalent for the Jupiter and Earth encounters. Without taking the frequencies of close encounters into account, massive planets such as Jupiter yield less precise density moment estimates.

[A3](#)) can be extended to include this extra mass, though this can only be done when the asteroid never passes inside the moon’s orbit. As an order-of-magnitude estimate for this effect, two spherical objects with masses and radii of Earth and the Moon, separated by one Lunar distance, and both lying in the orbital plane has a combined oblateness of $\epsilon = 0.82$. Extrapolating moment uncertainties via the slopes of the best fit lines given earlier yields a reduction in $\sigma(K_{2m})$ by about 25%. Furthermore, J_{22} is non-zero for this case, which likely decreases moment uncertainty even more.

This analysis suggests that large moons such as ours can improve fit quality, but further study of this effect (e.g., investigating an encounter that approaches both the Earth and the Moon closely) is beyond the scope of this paper.

4.3 Comparison of Jupiter and Earth encounters

If sufficiently accurate spin pole data can be detected for non-Earth encounters, it may be possible to extract density moments for encounters with larger planets. In this section, we run our reference asteroid through a Jupiter encounter to analyze the differences in uncertainty.

The physical parameters of the asteroid body are kept the same as the Earth encounter case, as are the observational uncertainty and cadence. The orbit is adjusted for the Jupiter case by setting a perijove distance of $r_p = 5$ Jupiter radii (compared to perigee radius $r_p = 5$ Earth radii for the Earth encounter). The excess velocity does not strongly affect $\sigma(K_{\ell m})$ as shown in figure 8, so we keep it at the reference value. The ratio between the moment uncertainties in the Jupiter and the Earth encounters are shown in table 2. In all cases, the Jupiter-encounter moments are more uncertain than Earth-encounter moments.

These uncertainty ratios can be understood as follows. The leading order of tidal torque is proportional to μ_A/D^3 . If D/a_B (the ratio of the encounter distance to the central body radius) is roughly constant as in this case, then $\mu_A/D^3 \propto \rho_B$ where ρ_B is the density of the central body. Therefore, little advantage is to be gained by looking for encounters of a massive planet in this sense. The second-order terms are damped by an additional factor of a_A/D , which decreases if a massive central body is used. Since Jupiter is about 10 times larger in radius than Earth, we expect that the K_{3m} terms are

about ten times more uncertain than the K_{2m} components, which is the case.

The $K_{\ell 0}$ components differ in that the moment uncertainty increase for a Jupiter encounter over an Earth encounter is about five times greater for $K_{\ell 0}$ than other moments of the same ℓ . In fact, K_{30} essentially fills the prior. In section 4.1.3, we note that $K_{\ell 0}$ is particularly uncertain when the asteroid does not tumble after the perigee. In this case, the Jupiter encounter resulted in less tumbling than the Earth encounter, so the larger increase in uncertainty in $K_{\ell 0}$ shown in table 2 is expected.

There are additional effects of central body mass which are not captured in this analysis. For example, encounters with massive planets are more plentiful, so that observation for a fixed period of time will lead to a larger number of observed encounters conducive to low-uncertainty moment extraction (small r_p , large a_A , etc.). This can be seen via the following equation for the area of the keyhole through which the asteroid must fly to have a perijove r_p or lower:

$$A = 2\pi r_p^2 \left(1 + 2 \frac{G\mu_B}{r_p v_\infty^2} \right). \quad (11)$$

Table 2 suggested that moment uncertainty is roughly $\sigma(K_{\ell m}) \propto a_B^{\ell-1}/r_p$, so that constant uncertainty roughly implies $r_p \propto a_B^{1/2}$. Since $a_B \sim \mu_B^{1/3}$, equation 11 dictates that b/r_p will increase faster than a_B as μ_B is increased. It follows that the number of encounters that meet the uncertainty threshold will grow substantially. Other effects, such as a change in the physical properties of the encountering asteroids or decreased observational uncertainty due to the distance between Jupiter and Earth-based telescopes, may also affect the fit uncertainties. Which of these contradicting effects dominates depends on the asteroid population near Jupiter and the observation method.

4.4 Comparisons between density distribution models

In section 3.2, we displayed uniform and non-uniform density distributions extracted via the finite element and single-lump lumpy model. Here we highlight the properties of the model in two other scenarios.

Figure 12 shows density distributions extracted via the finite element model and the lumpy model for a centred core of density three times the surrounding density. Results are similar to the off-center core shown in 5 in that the moments of the resulting density distribution are consistent with those extracted from the encounter data (i.e., χ_r^2 is low). Again, the finite element model does not isolate the lump, instead spreading the excess mass over the asteroid. Unlike the off-center core example, the lumpy model is not able to recover the true distribution either. It produces deviations from the true density distribution of roughly the same size as the finite element model, with large significance. This is because, for centred, spherical cores, the core mass is degenerate with the core’s radius.

The success of the model in the off-center case was due to the fact that the shape of the asteroid was offset from the center of mass by a corresponding amount, assumed to be known precisely. The position of the lump was therefore observed up to one free parameter: the lump’s mass. The assumption that the asteroid’s center of mass is so precisely

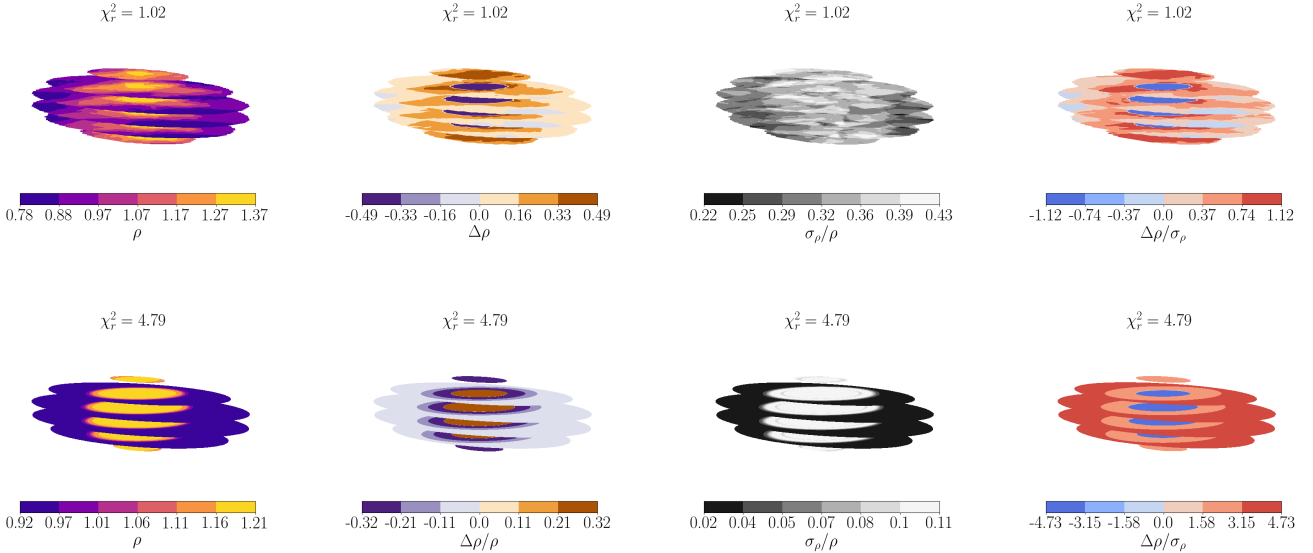


Figure 12. Cross-sectional slices of the density distributions extracted via the finite-element (*top*) and lumpy (*bottom*) models for an asteroid with a centred core. From left to right, the densities, deviations from the true density, uncertainties, and significance of the deviations are plotted. These figures are available in animated form in appendix figure D3. The resulting density distribution is consistent with the density moments but does not represent the true distribution due to degeneracy.

known stems from the fact that the shape of the asteroid is observed to rotate around its center of mass. If observations do not allow the center of mass to be determined in this way, then the lump's position will be more uncertain for the off-center case.

To assess the lumpy model when the positions of the lump are not as certain as in the off-center case, we consider an asteroid with two lumps of radii 300 m and density three times the surrounding density. Each lump is located 500 meters from the center of the asteroid, so that they counterbalance and the asteroid's observed center of mass is its surface's centroid. The corresponding two-lump lumpy model has seven DOF, in contrast to the 5 DOF of the finite element model. Both models are run on this asteroid and the resulting distributions are shown in figure 13.

Figure 13 again shows that the finite element model is unable to isolate the lumps except to predict generally increased density near the center. On the other hand, the lumpy model detects that the two lumps are opposite each other, and of roughly the same radius and mass. These radius and mass values are also close to the true values. The model places the lumps correctly in the xy -plane of the asteroid but does not perfectly align them with the y axis, resulting in high $\Delta\rho$ where the true lumps and predicted lumps do not intersect. Uncertainty is also high, due to the extra DOF. Note that χ^2_r remains low despite the lumpy model's misplacement of the lumps. This is because the lumpy model gains its information on the placement of the lumps from the K_{3m} density moments, which figures 8 and 9 suggest are not as well constrained as the K_{2m} density moments. The high uncertainty results in a deviation of a few hundred meters in lump location for the reference encounter properties.

5 CONCLUSIONS

We derived a novel, arbitrary-order equation for the tidal torque experienced by an asteroid during an encounter with a planet of arbitrary shape and mass distribution. The tidal torque (equation 4) revealed that the angular velocity of the asteroid over time depends strongly on the asteroid's density moments and the initial orientation. We then built a fast simulation for an asteroid encounter and designed an MCMC to extract density moments from simulated data. We also created two models — the finite element model and the lumpy model — to translate these density moments back into density distributions. Uncertainties are propagated throughout the pipeline. Since the density distribution inverse problem is underdetermined, the models give different results and were contrasted. Nevertheless, we find that the models always produce results consistent with the data set and usually consistent with the true distribution.

We assessed the uncertainty of the pipeline's results by adjusting various properties of the asteroid and its Earth encounter. The thresholds we measure (table 1) show that the observational uncertainty and perigee of the asteroid orbit have the strongest effect on the density distribution uncertainty and they are the most important thresholds to meet in order to extract a precise distribution. The properties that do not affect density uncertainty as much, such as the central body oblateness, must still be accurately represented in simulations to avoid errors in the pipeline results. We also discussed how these thresholds could be eased by changes in observational behaviour such as lengthening the data set, or by physical asteroid properties such as a closer encounter, an initially tumbling state, or the presence of a massive moon such as Earth's. If the thresholds were eased enough, then the asteroid length would become an important threshold as well.

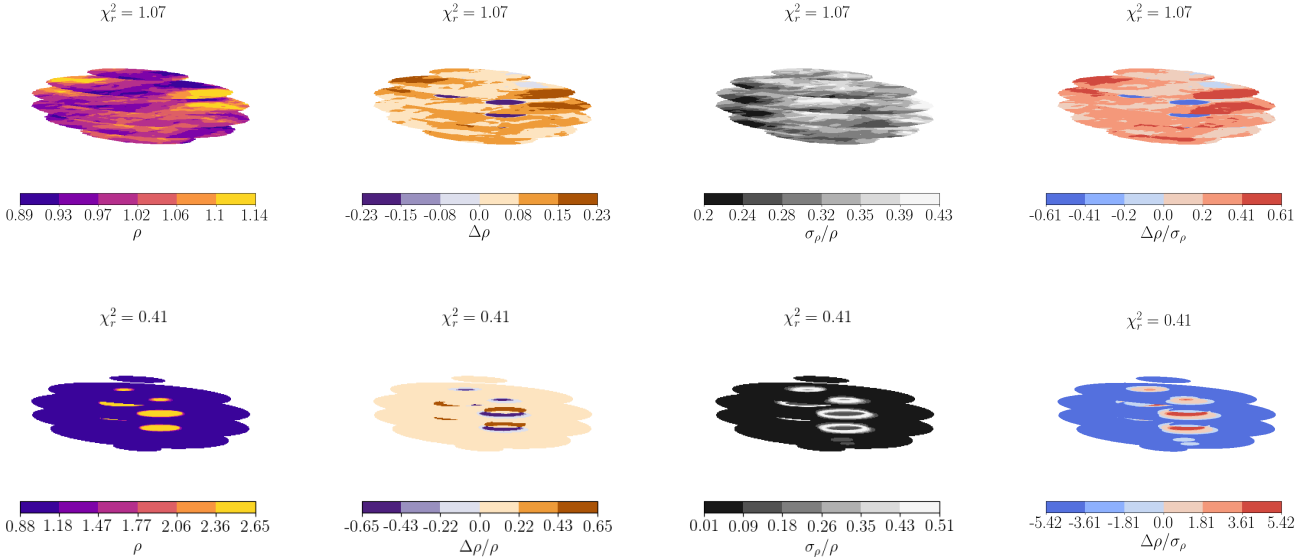


Figure 13. Cross-sectional slices of the density distributions extracted via the finite-element (*top*) and the two-lump lumpy (*bottom*) models for an asteroid with two counterbalancing cores. From left to right, the densities, deviations from the true density, uncertainties, and significance of the deviations are plotted. These figures are available in animated form in appendix figure D4. The additional lump greatly increases uncertainty, but the resulting distribution is close to accurate.

Finally, we highlighted that the properties of the final density distribution are strongly model-dependent. The uncertainties on density distribution of the two models were drastically different, and also depended on the number of degrees of freedom used in the model. For asteroids of non-uniform distributions, the distributions themselves also differed. To efficiently use encounter data, it is therefore important to investigate multiple models and choose different models to answer different questions, such as the lumpy model to look for discrete regions of increased density.

ACKNOWLEDGEMENTS

We warmly thank Emmanuel Jehin, Maxime Devogele, and Marin Ferrais for meeting with the authors to discuss this work and pointing out possible future initiatives. JTD also thanks the MIT UROP office for funding his work. This paper made substantial use of MIT Supercloud’s facilities.

DATA AVAILABILITY

The asteroid simulation, fit process, and density moment extraction code are available on [GitHub](#). Please contact JTD with questions.

REFERENCES

- Ashenberg J., 2007, *Celestial Mechanics and Dynamical Astronomy*, 99, 149
- Benson C. J., Scheeres D. J., Moskovitz N. A., 2020, *Icarus*, 340, 113518
- Berthier J., et al., 2020, *Icarus*, 352, 113990
- Boué G., Laskar J., 2009, *Icarus*, 201, 750
- Brown T., et al., 2013, *Publications of the Astronomical Society of the Pacific*, 125, 1031
- Carroll K., Faber D., 2018, in *Proceedings of the 69th International Astronautical Congress*.
- Descamps P., et al., 2020, *Icarus*, 345, 113726
- Devogèle M., et al., 2021, *Monthly Notices of the Royal Astronomical Society*, 505, 245
- Foreman-Mackey D., Hogg D. W., Lang D., Goodman J., 2013, *Publications of the Astronomical Society of the Pacific*, 125, 306
- Gao F., Han L., 2012, *Computational Optimization and Applications*, 51, 259
- Giorgini J., Benner L., Nolan M., Ostro S., 2005, in *AAS/Division of Dynamical Astronomy Meeting# 36*. pp 02–01
- Giorgini J. D., Benner L. A., Ostro S. J., Nolan M. C., Busch M. W., 2008, *Icarus*, 193, 1
- Hirabayashi M., Kim Y., Brozović M., 2021, *Icarus*, 365, 114493
- Hou X., Scheeres D. J., Xin X., Mar 2017, *Celestial Mechanics and Dynamical Astronomy*, 127, 369
- Kaasalainen M., 2001, *Astronomy & Astrophysics*, 376, 302
- Kaiser N., et al., 2002, in *Survey and Other Telescope Technologies and Discoveries*. pp 154–164
- Larson S., Brownlee J., Hergenrother C., Spahr T., 1998, in *Bulletin of the American Astronomical Society*. p. 1037
- Lee H.-J., et al., 2022.
- Makarov V. V., Goldin A., Tkachenko A. V., Veras D., Noyelles B., 2022.
- Moskovitz N. A., et al., 2020, *Icarus*, 340, 113519
- Naidu S. P., Margot J.-L., 2015, *The Astronomical Journal*, 149, 80
- Pater D. I., Lissauer J. J., 2015, *Planetary sciences*, 2 edn. Cambridge University Press
- Paul M. K., 1988, *Celestial mechanics*, 44, 49
- Pravec P., et al., 2014, *Icarus*, 233, 48
- Richardson D. C., Bottke W. F., Love S. G., 1998, *Icarus*, 134, 47
- Richardson J. E., Melosh H. J., Greenberg R. J., O’Brien D. P., 2005, *Icarus*, 179, 325
- Scheeres D., Ostro S., Werner R., Asphaug E., Hudson R., 2000,

- Icarus*, 147, 106
 Scheeres D. J., Marzari F., Rossi A., 2004, *Icarus*, 170, 312
 Smalley K., Garradd G., Benner L., Nolan M., Giorgini J., Chesley S., Ostro S., Scheeres D., 2005, International Astronomical Union Circular, 8477, 1
 Souchay J., Souami D., Lhotka C., Puente V., Folgueira M., 2014, *Astronomy & Astrophysics*, 563, A24
 Souchay J., Lhotka C., Heron G., Herve Y., Puente V., Lopez M. F., 2018, *Astronomy & Astrophysics*, 617, A74
 Stokes G. H., Evans J. B., Viggh H. E., Shelly F. C., Pearce E. C., 2000, *Icarus*, 148, 21
 Tyson J. A., 2002, *Survey and Other Telescope Technologies and Discoveries*, 4836, 10
 Valvano G., Winter O. C., Sfair R., Machado Oliveira R., Borderes-Motta G., Moura T., 2022, *Monthly Notices of the Royal Astronomical Society*, 510, 95
 Wright E. L., et al., 2010, *The Astronomical Journal*, 140, 1868
 Yu Y., Richardson D. C., Michel P., Schwartz S. R., Ballouz R.-L., 2014, *Icarus*, 242, 82
 van Gelderen M., 1998, in *The shift operators and translations of spherical harmonics*.

APPENDIX A: TIDAL TORQUE & EQUATIONS OF MOTION

In this appendix, we derive the equations of motion used to simulate the asteroid angular velocity during the encounter. In particular, we describe our coordinates (section A1) for an encountering asteroid's position and orientation, and we parametrize its density distribution via its density moments (section A2). Then we derive an arbitrary-order equation for tidal torque (section A3) and write the equations of motion for the system (section A4).

A1 Coordinates

We make use of two frames of reference to model this system. One is the “inertial frame,” with axes denoted by $\hat{\mathbf{X}}, \hat{\mathbf{Y}}, \hat{\mathbf{Z}}$ and origin placed at the central body’s centre of mass. $\hat{\mathbf{X}}$ points from the central body to the asteroid perihelion, and $\hat{\mathbf{Z}}$ points parallel to the orbit angular momentum. We assume that the mass distribution of the central body is known in this inertial frame.

Our second frame is the “body-fixed” frame, denoted by $\hat{\mathbf{x}}, \hat{\mathbf{y}}, \hat{\mathbf{z}}$. Each axis in this frame is aligned with a principal axis and rotates with the asteroid, with its origin at the asteroid’s centre of mass. For definiteness, we define $\hat{\mathbf{z}}$ to be the principal axis with maximal MOI (this is the short axis mode, to use the vocabulary of Ref. Kaasalainen (2001)). In general, we use capital letters to denote vectors in the inertial frame and lowercase vectors to denote vectors in the body-fixed frame.

The difference between the origins of the body-fixed and inertial frames is the position of the asteroid. We represent the relative orientations by $z - y - z$ Euler angles α, β , and γ , such that a matrix M rotating from the body-fixed to the inertial frame ($M\mathbf{r} = \mathbf{R}$) is given by

$$M = R_z(\alpha)R_y(\beta)R_z(\gamma). \quad (\text{A1})$$

Here, $R_i(\theta)$ is a rotation around the unit vector i by θ (figure A1).

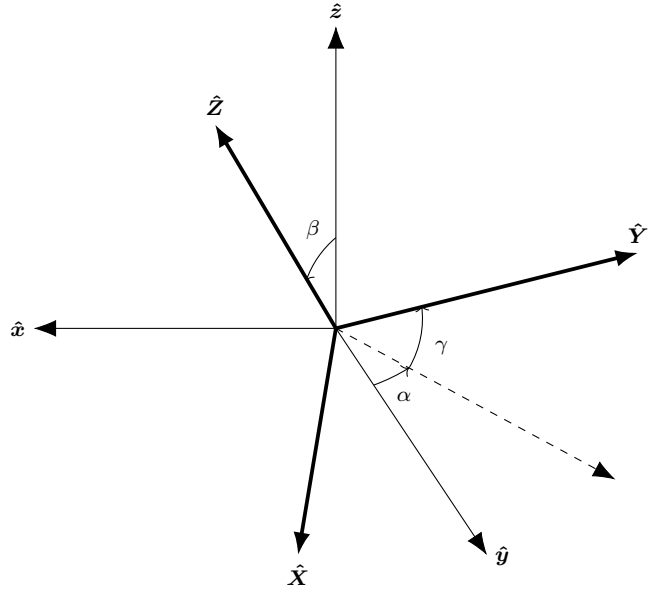


Figure A1. $z - y - z$ Euler angles used in this work to express the orientation of the asteroid. Orientation is expressed as a rotation from the body-fixed axes (lowercase) to the inertial axes (bold lines and uppercase). The origins are co-located for demonstration purposes.

A2 Density moments

The un-normalized spherical harmonics are defined as $Y_{\ell m}(\theta, \phi) = P_{\ell m}(\cos \theta)e^{im\phi}$, where $P_{\ell m}$ are the associated Legendre Polynomials without the Condon-Shortley phase. The regular and irregular spherical harmonics are further defined as

$$\begin{aligned} S_{\ell m}(\mathbf{r}) &= (-1)^m (\ell - m)! \frac{Y_{\ell m}(\hat{\mathbf{r}})}{r^{\ell+1}} \\ R_{\ell m}(\mathbf{r}) &= (-1)^m \frac{r^\ell}{(\ell + m)!} Y_{\ell m}(\hat{\mathbf{r}}). \end{aligned} \quad (\text{A2})$$

These spherical harmonics obey many useful identities summarized in Ref. van Gelderen (1998), which are also useful for quantum mechanics. They were used to define the density moments in equation 1, which can be extended to the central body:

$$J_{\ell m} = \frac{a_B^{2-\ell}}{I_B} \int_B d^3 r \rho_B(\mathbf{r}) R_{\ell m}(\mathbf{r}) \quad (\text{A3})$$

By contrast, $J_{\ell m}$ should be computed in the inertial frame. The length scale a_B and MOI scale I_B can be defined similarly to a_A and a_B in equations 3 and 2, but they could also be set to any other scales of the same units, e.g. a_B equal to the central body radius and $I_B = \mu_B a_B^2$, where μ_B is the central body mass.

Note that both $J_{\ell m}$ and $K_{\ell m}$ are unitless. We call them “moments” because the $R_{\ell m}(\mathbf{r})$ contains an r^ℓ dependence so that $K_{\ell m}$ is the ℓ th density moment of the asteroid.

These moments share several key properties which we discuss before continuing. Firstly, for real mass density, properties of the spherical harmonics imply that $K_{\ell m} = (-1)^m K_{\ell, -m}^*$. Therefore, the set of $K_{\ell m}$ for $\ell < \ell_{\max}$ contains ℓ_{\max}^2 degrees of freedom. However, some of these degrees of freedom are redundant with the choice of coordinates: $K_{1m} = 0$ since the body-fixed frame is centred on the

ℓ	$\Re K_{\ell 3}$	$\Im K_{\ell 3}$	$\Re K_{\ell 2}$	$\Im K_{\ell 2}$	$\Re K_{\ell 1}$	$\Im K_{\ell 1}$	$K_{\ell 0}$
0							-
1				x	y	z	
2			-	x,y	y,z	x,z	-
3	x,z	y,z	z	x,y,z	x	y	z

Table A1. Axes of mirror symmetry that imply zeroed density moments. For example, for mirror symmetries along $\hat{\mathbf{y}}$ or $\hat{\mathbf{z}}$, $\Im K_{32} = 0$. Mirror symmetry along $\hat{\mathbf{x}}$ means $\rho_{\mathcal{A}}(x, y, z) = \rho_{\mathcal{A}}(-x, y, z)$. Dashes indicate that none of the mirror symmetries zero the moment in question. Since $r^2 > 0$ for $r \neq 0$, no symmetries set $a_{\mathcal{A}} = 0$ either.

asteroid centre of mass. Further calculation reveals that the alignment of the body-fixed frame with the asteroid principal axes also forces $K_{21} = 0$ and $\Im K_{22} = 0$. The only physical density moments for $\ell \leq 2$ are therefore K_{22} , K_{20} , and K_{00} . The first two are related to the MOI around each principal axis by equation 5, while $K_{00} = \mu_{\mathcal{A}} a_{\mathcal{A}}^2 / I_{\mathcal{A}}$ will not be relevant to this study as it does not appear in equation 4.

The physical meaning of K_{22} and K_{20} can also be interpreted via a special case: if the asteroid is a uniform-density triaxial ellipsoid, the moments of inertia are simple to compute in terms of the semi-axis lengths and can be compared to those found in equation 5. This yields semi-axis lengths of

$$\begin{aligned} a &= \sqrt{\frac{5}{3}} a_{\mathcal{A}} \sqrt{1 - 2K_{20} + 12K_{22}} \\ b &= \sqrt{\frac{5}{3}} a_{\mathcal{A}} \sqrt{1 - 2K_{20} - 12K_{22}} \\ c &= \sqrt{\frac{5}{3}} a_{\mathcal{A}} \sqrt{1 + 4K_{20}}. \end{aligned} \quad (\text{A4})$$

The higher-order moments K_{3m} can be thought of loosely as measuring the large-scale asymmetries of the asteroid. An asteroid that is mirror-symmetric along the $\hat{\mathbf{x}}$ axis (meaning $\rho_{\mathcal{A}}(x, y, z) = \rho_{\mathcal{A}}(-x, y, z)$) necessarily sets certain density moments to zero. Which density moments are zeroed by which mirror symmetries is outlined in table A1. All K_{3m} are zeroed by at least one mirror symmetry.

Finally, the requirement that $\rho_{\mathcal{A}}(\mathbf{r}) \geq 0$ everywhere restricts $K_{\ell m}$. In the case of K_{2m} , this fact and the constraint that I_z is larger than I_x or I_y requires K_{20} and K_{22} to fall in the triangle

$$-\frac{1}{4} \leq K_{20} \leq 0, \quad |K_{22}| \leq -\frac{K_{20}}{2}. \quad (\text{A5})$$

An analytical constraint on K_{3m} based on this property is more difficult to derive, but in practice, we also observe that $|K_{3m}| < 0.01$.

A3 Tidal torque

Derivations for the tidal torque experienced by a rigid body in the gravitational field of a larger mass have been computed by several previous studies Paul (1988); Hou et al. (2017); Boué & Laskar (2009); Ashenberg (2007), often in terms of the MOI of the rigid body (or higher order moments of inertia), and to varying degrees of precision. A simple, first-order derivation is also easily computable in terms of the asteroid MOI in the inertial frame.

Here, we present a new derivation of the tidal torque to

arbitrary orders in terms of the density moments of an asteroid defined in section A2. These density moments can be pre-computed and do not have to be re-evaluated every timestep.

The gravitational potential energy of the central body is, in its most general form,

$$V(\mathbf{R}') = -G \int_{\mathcal{B}} d^3 R \rho_{\mathcal{B}}(\mathbf{R}) \frac{1}{|\mathbf{R} - \mathbf{R}'|}. \quad (\text{A6})$$

where $\rho_{\mathcal{B}}$ is the density distribution of the central body and \mathcal{B} indicates the central body's volume. All vectors here are written in the inertial frame. Given $|\mathbf{R}| < |\mathbf{R}'|$, Ref. van Gelderen (1998) gives the identity

$$\frac{1}{|\mathbf{R} - \mathbf{R}'|} = \sum_{\ell, m} R_{\ell m}(\mathbf{R}) S_{\ell m}^*(\mathbf{R}'), \quad (\text{A7})$$

where the sum is shorthand for $\sum_{\ell, m} = \sum_{\ell=0}^{\infty} \sum_{m=-\ell}^{\ell}$.

Incidentally, it is the $|\mathbf{R}| < |\mathbf{R}'|$ assumption that inspires the assumption that there are “no distant perturbing objects” (section 2). If a perturbing object such as a moon is not distant (i.e., it is closer to the system center of mass than the asteroid perigee so that $|\mathbf{R}| < |\mathbf{R}'|$ always), then it can be absorbed into $J_{\ell m}$ by equation A3 and the assumptions of this derivation are not violated.

We are interested in translating the potential energy of equation A6 to the body-fixed frame. To do this, we let $\mathbf{R}' = \mathbf{D} + \mathbf{U}$, where \mathbf{D} is the location of the asteroid in the inertial frame. We further define $\mathbf{U} = M\mathbf{u}$, where \mathbf{u} is in the body-fixed frame and M is the rotation matrix given by the Euler angles α , β , and γ (see section A1). The translation from \mathbf{R}' to \mathbf{U} is then attained by the identity

$$S_{\ell m}(\mathbf{R}') = \sum_{\ell', m'} (-1)^{\ell'} R_{\ell' m'}^*(\mathbf{U}) S_{\ell + \ell', m + m'}(\mathbf{D}), \quad (\text{A8})$$

provided by Ref. van Gelderen (1998), and from \mathbf{U} to \mathbf{u} is given by

$$\begin{aligned} Y_{\ell m}(M\mathbf{u}) &= \sum_{m'=-\ell}^{\ell} (-1)^{m+m'} \sqrt{\frac{(\ell - m')!(\ell + m)!}{(\ell + m')!(\ell - m)!}} \\ &\times \mathcal{D}_{mm'}^{\ell}(M)^* Y_{\ell m'}(\mathbf{u}). \end{aligned} \quad (\text{A9})$$

Here, $\mathcal{D}_{mm'}^{\ell}(M)$ are the Wigner-D matrices, which are determined by the Euler angles α , β , and γ of M .

Equations A6 to A9 then provide formula for $V(\mathbf{u})$ expressed as a sum of integrals over \mathcal{B} of the central body density $\rho_{\mathcal{B}}(\mathbf{R})$ times $R_{\ell m}(\mathbf{R})$. These are expressed via equation A3 as $J_{\ell m}$.

The tidal torque experienced by the asteroid (in the body-fixed frame) is given by

$$\boldsymbol{\tau}(\mathbf{u}) = \int_{\mathcal{A}} d^3 u \rho_{\mathcal{A}}(\mathbf{u}) (\mathbf{u} \times (-\nabla_{\mathbf{u}} V(\mathbf{u}))) \quad (\text{A10})$$

where $\rho_{\mathcal{A}}$ is the density distribution of the asteroid and \mathcal{A} indicates the volume of the asteroid. Making use of one more identity concerning the derivatives of spherical harmonics:

$$\begin{aligned} \mathbf{u} \times \nabla R_{\ell m}(\mathbf{u}) &= \frac{1}{2} \left[(i\hat{\mathbf{x}} - \hat{\mathbf{y}})(\ell - m + 1) R_{\ell, m-1}(\mathbf{u}) \right. \\ &\quad + (i\hat{\mathbf{x}} + \hat{\mathbf{y}})(\ell + m + 1) R_{\ell, m+1}(\mathbf{u}) \\ &\quad \left. + 2im\hat{\mathbf{z}} R_{\ell m}(\mathbf{u}) \right], \end{aligned} \quad (\text{A11})$$

tidal torque can now be expressed as a function only of the

constants $J_{\ell m}$, $K_{\ell m}$, $a_{\mathcal{A}/\mathcal{B}}$, $I_{\mathcal{A}/\mathcal{B}}$, and the asteroid orientation and position (equation 4). Some $K_{\ell m}$ terms are written in this equation with $|m| > \ell$; these should all be taken to be zero.

A4 Equations of motion

The equations of motion of the asteroid position \mathbf{D} are given by Newton's law of gravitation

$$\dot{\mathbf{V}} = -\frac{G\mu_{\mathcal{B}}}{D^3} \mathbf{D} \quad \dot{\mathbf{D}} = \mathbf{V} \quad (\text{A12})$$

where \mathbf{V} is the asteroid velocity in the inertial frame. Rather than derive equations of motion for the Euler angles (which suffer from gimbal lock), we instead represent the orientation of the asteroid with a quaternion $\tilde{\mathbf{q}}$ which can be converted into Euler angles to compute $\mathcal{D}(\alpha, \beta, \gamma)$. This quaternion evolves as

$$\dot{\tilde{\mathbf{q}}} = \frac{1}{2}\tilde{\mathbf{q}}\tilde{\boldsymbol{\omega}}. \quad (\text{A13})$$

for angular velocity $\boldsymbol{\omega}$ given in the body-fixed frame. The equations of motion of $\boldsymbol{\omega}$ in turn are given by

$$\begin{aligned} I_x \dot{\omega}_x - \omega_y \omega_z (I_y - I_z) &= \tau_x \\ I_y \dot{\omega}_y - \omega_z \omega_x (I_z - I_x) &= \tau_y \\ I_z \dot{\omega}_z - \omega_x \omega_y (I_x - I_y) &= \tau_z. \end{aligned} \quad (\text{A14})$$

Equations 4, 5, and A12 to A14 form a set of non-linear, first-order coupled differential equations in which can be numerically integrated. They are expressed in terms of the physical parameters $I_{\mathcal{A}/\mathcal{B}}$, $a_{\mathcal{A}/\mathcal{B}}$, $J_{\ell m}$, and $K_{\ell m}$ which are constant if the asteroid is rigid and the central body does not rotate.

APPENDIX B: ADDITIONAL DENSITY DISTRIBUTION MODELS

Two models were discussed in section 2.4 to translate density moment constraints into density distribution constraints. Here we outline two additional models, the nearly-uniform and the harmonic models, which are less conventional but still useable for extracting density distribution properties. Unlike the finite element and lumpy models discussed in the main text, these models will yield smooth distributions with no discrete transitions. They also rely on a known surface for the asteroid.

B1 Nearly-uniform model

In this “nearly-uniform” model, we seek to pick one density distribution from the many distributions consistent with the data by maximizing a prior distribution $f[\rho(\mathbf{r})]$, which can be chosen manually. Any prior distribution can be chosen, but the following prior is both interesting and numerically efficient.

As part of our prior, we require that the asteroid density distribution satisfy $I_{\mathcal{A}} = \mu_{\mathcal{A}} a_{\mathcal{A}}^2$. This constraint is desirable as it is obeyed for uniform density distributions. To define the prior, we divide the asteroid into $n \gg 1$ small regions of volume V , each with position \mathbf{r}_i and density $\rho_i = \delta_i + 1$. Setting the mass of the asteroid equal to its volume, the average density is 1, so δ_i is the difference between the average and local

density. We set $f[\rho(\mathbf{r})]$ to be a multivariate-Gaussian distribution on δ_i , centred on zero to minimize non-uniformity, i.e.

$$f[\rho(\mathbf{r})] \propto \prod_i \exp\left(-\frac{\delta_i^2}{2\sigma^2}\right) \implies \ln f[\rho(\mathbf{r})] \simeq -\sum_i \delta_i^2 \quad (\text{B1})$$

where σ is an irrelevant constant. The density moments, MOI scale, and mass are

$$K_{\ell m} = \frac{V}{\mu_{\mathcal{A}} a_{\mathcal{A}}^{\ell}} \sum_i (\delta_i + 1) R_{\ell m}(\mathbf{r}_i) \quad (\text{B2})$$

$$I_{\mathcal{A}} = \mu_{\mathcal{A}} a_{\mathcal{A}}^2 = V \sum_i (\delta_i + 1) r_i^2 \quad (\text{B3})$$

$$\mu_{\mathcal{A}} = V \sum_i (\delta_i + 1) \implies 0 = \sum_i \delta_i. \quad (\text{B4})$$

Writing δ_i as an n -dimensional vector $\boldsymbol{\delta}$, equation B2 is a matrix equation for $K_{\ell m}$, and equations B3 and B4 are vector dot product equations. Combining $K_{\ell m}$, $I_{\mathcal{A}}$, and 0 into a single vector \mathbf{K} , these equations can be written as a single underdetermined matrix equation we denote as

$$\mathbf{K} = M\boldsymbol{\delta} + \mathbf{C}, \quad (\text{B5})$$

where the components of constant matrix M and constant vector \mathbf{C} are known given a fixed layout of the n regions. Some of the components of \mathbf{K} , such as $I_{\mathcal{A}}$, $\mu_{\mathcal{A}}$, and K_{1m} , are constraints. We treat the other components as parameters of the model. The task is then to find $\boldsymbol{\delta}$ that satisfies equation B5 and maximizes $f(\boldsymbol{\delta})$. But the form of equation B1 shows that the maximum of $\ln f$ (also the maximum of f) is the minimum of $|\boldsymbol{\delta}|^2$. This shortest value of $\boldsymbol{\delta}$ that obeys equation B5 is given by the Moore-Penrose inverse:

$$\boldsymbol{\delta} = M^+ (\mathbf{K} - \mathbf{C}); \quad M^+ = M^\dagger (M M^\dagger)^{-1} \quad (\text{B6})$$

where M^\dagger is the adjoint of M .

The prior distribution on $\rho(\mathbf{r})$ discussed in section 2.3 can be implemented by individually checking the components $\boldsymbol{\delta}$ computed by equation B6 and confirming that $1 + \delta_i$ lies within the acceptable range of densities. can be implemented by individually checking the components $\boldsymbol{\delta}$ computed by equation B6 and confirming that $1 + \delta_i$ lies within the acceptable range of densities.

B2 Harmonic model

This the “harmonic model”, we limit ourselves to density distributions that are harmonic; i.e., they satisfy $\nabla^2 \rho(\mathbf{r}) = 0$. We have no physical justification for why this assumption should be true, but it is useful as a simplification to gain qualitative insight into the properties of the asteroid density distribution.

A harmonic density distribution can be expanded in terms of the spherical harmonics as $\rho(\mathbf{r}) = \sum_{\ell m} C_{\ell m} R_{\ell m}(\mathbf{r})^*$ where $C_{\ell m}$ are complex, free parameters. This series can be truncated at some maximum ℓ . The density moments, MOI scale, and mass can then be explicitly computed as a function of $C_{\ell m}$:

$$K_{\ell m} = \frac{a_{\mathcal{A}}^{2-\ell}}{I_{\mathcal{A}}} \sum_{\ell m} C_{\ell' m'} \int_{\mathcal{A}} d^3 r R_{\ell' m'}(\mathbf{r})^* R_{\ell m}(\mathbf{r}) \quad (\text{B7})$$

$$I_{\mathcal{A}} = \sum_{\ell m} C_{\ell m} \int_{\mathcal{A}} d^3 r R_{\ell m}(\mathbf{r})^* r^2 \quad (\text{B8})$$

$$\mu_{\mathcal{A}} = \sum_{\ell m} C_{\ell m} \int_{\mathcal{A}} d^3 r R_{\ell m}(\mathbf{r})^*. \quad (\text{B9})$$

These integrals can be pre-computed given a known asteroid shape \mathcal{A} , so that computing $C_{\ell m}$ to match a given $K_{\ell m}$ is fast. Furthermore, their values when \mathcal{A} is spherical gives us insight into the influence of $K_{\ell m}$ on density distributions. In this case, $I_{\mathcal{A}} \propto C_{00}$ and the integral of equation B7 is non-zero only when $\ell' = \ell$ and $m' = m$. Therefore, $C_{\ell m}$ is proportional to $K_{\ell m}$. The density distribution can be immediately visualized given the density moments as a sum of the solid spherical harmonics weighted by $K_{\ell m}$. When the asteroid is non-spherical, the shape itself contributes to $K_{\ell m}$ so as to break this picture.

Imposing constraints on these moments is also necessary. The choice of mass is enforced via equation B9. We impose bounds on $\rho(\mathbf{r})$ by acknowledging that harmonic functions such as $\rho(\mathbf{r})$ in a region such as \mathcal{A} attain their maxima on the boundary of the region, so that it is only necessary to ensure that ρ lies within the allowed range on the asteroid boundary rather than within the entire asteroid. This can be done by parametrizing the asteroid surface as a function of two variables (e.g., latitude and longitude) and minimizing and maximizing ρ with respect to those variables, ensuring these minima and maxima are within the allowed range.

APPENDIX C: COMPARING ORIENTATION AND ANGULAR VELOCITY DATA

To extract the density distribution of an asteroid, the main text assumes that the angular velocity data of the asteroid is observable. It is possible that the orientation of the asteroid may be better constrained by observations than angular velocity. In this appendix, we generate an orientation data set for the reference asteroid flyby, extract a density distribution from it, and compare the results to distributions extracted from angular velocity data.

We may expect some differences in the resolving power of orientation and angular velocity data, but not a large difference, due to the following argument. If the initial orientation of the asteroid is known, then the orientation of the next data point can be determined by knowledge of the asteroid's angular velocity at that moment. Thus, an orientation data set can be produced from an angular velocity data set and vice versa given an initial asteroid position. The initial position is defined up to γ_0 by the assumption of no initial tumbling, and figures 8 and 9 reveal that γ_0 is typically also constrained to high precision even by angular velocity data. Thus, we expect the only differences between moment uncertainty as obtained from angular velocity data or from orientation data to be due to the uncertainty of the data itself.

C1 Uncertainty model

The likelihood used by the MCMC (equation 7) requires redefinition in order to extract density moments from orienta-

Figure C1. JTD: Write

tion data. This requires a new model for the uncertainty of orientation observations.

For the sake of this appendix, we will assume that all observations of orientation O differ from the true orientation O^* by a rotation by some angle ϕ around an axis drawn from a uniform distribution on the unit sphere, where ϕ is drawn from a normal distribution with mean zero and standard deviation σ_ϕ . Expressing orientation as a quaternion $\tilde{\mathbf{q}} = q_r + q_i \mathbf{i} + q_j \mathbf{j} + q_k \mathbf{k}$, ϕ can be extracted and the likelihood written as

$$\ln \mathcal{L} = -\frac{2}{\sigma_\phi^2} \sum_{i=0}^n \left(\cos^{-1} [(\tilde{\mathbf{q}}_i (\tilde{\mathbf{q}}_i^*)^{-1})_r] \right)^2 \quad (\text{C1})$$

where $\tilde{\mathbf{q}}_i$ is the i th quaternion in the data set measured in the inertial frame, and $\tilde{\mathbf{q}}_i^*$ is the true quaternion. It is assumed that both quaternions have norm one.

C2 Moment uncertainty comparison

With the likelihood defined, density moments can be extracted from the orientation data via the fit process described in the main text and compared to those extracted from the angular velocity data. We generate data of both types for the reference asteroid configuration and extract $K_{\ell m}$ means and uncertainties for both data sets.

Due to the different uncertainty models used for the orientation and angular velocity data sets, this set-up does not allow direct comparison between the sizes of moment uncertainty for both data sets. One could not tell if one data set yields more precise moments because the observational precision of that data set is better or because that data type affords better estimation of density moments. However, the relative uncertainty of moments can be compared between the two data sets.

We generate moment uncertainty for the orientation data using a test value of $\sigma_\phi = 0.1$ and compute the mean uncertainty. We then scale the moment uncertainties attained from the angular velocity data set with the reference observational uncertainty parameters so that the mean uncertainty of all the moments is equal to that of the orientation data set. This is equivalent to simply choosing observational uncertainties for the angular velocity data set which yield density moments to the same precision as the observational data set, because figure 9 shows that density moment uncertainty $\sigma(K_{\ell m})$ is proportional to observational uncertainty. We then compute the ratio between $\sigma(K_{\ell m})$ for the observational data set and the angular velocity data set and show the result as a function of ℓ and m in figure C1.

C3 Density uncertainty comparison

APPENDIX D: ANIMATED DENSITY DISTRIBUTIONS

This appendix contains animations to better display the density distributions shown in the main text. Each frame represents a cross section perpendicular to the $\hat{\mathbf{z}}$ -axis, starting with negative z and ending with positive z . All densities are divided by the mean asteroid density.

Please see the published version of the paper for these animations, or find them online at the following links.			
FE asymmetric density	FE asymmetric deviation	FE asymmetric uncertainty	FE asymmetric significance
Lumpy asymmetric density	Lumpy asymmetric deviation	Lumpy asymmetric uncertainty	Lumpy asymmetric significance
FE symmetric density	FE symmetric deviation	FE symmetric uncertainty	FE symmetric significance
Lumpy symmetric density	Lumpy symmetric deviation	Lumpy symmetric uncertainty	Lumpy symmetric significance

Figure D1. Density distributions extracted via the finite element model for the asymmetric (*top two rows*) and symmetric (*bottom two rows*) reference asteroids. The finite element model (*first and third rows*) and the lumpy model (*second and fourth rows*) are employed. From left to right, the densities, deviations from the true density, uncertainties, and significance of the deviations are plotted. Animated form of figure 4.

Please see the published version of the paper for these animations, or find them online at the following links.			
FE density	FE deviation	FE uncertainty	FE significance
Lumpy density	Lumpy deviation	Lumpy uncertainty	Lumpy significance

Figure D2. Density distributions extracted via the finite-element (*top*) and lumpy (*bottom*) models for an asteroid with an off-center core. From left to right, the densities, deviations from the true density, uncertainties, and significance of the deviations are plotted. Animated form of figure 5.

Please see the published version of the paper for these animations, or find them online at the following links.			
FE density	FE deviation	FE uncertainty	FE significance
Lumpy density	Lumpy deviation	Lumpy uncertainty	Lumpy significance

Figure D3. Density distributions extracted via the finite-element (*top*) and lumpy (*bottom*) models for an asteroid with a centred core. From left to right, the densities, deviations from the true density, uncertainties, and significance of the deviations are plotted. Animated form of figure 12.

This paper has been typeset from a TeX/LaTeX file prepared by the author.

Please see the published version of the paper for these animations, or find them online at the following links.

FE density	FE deviation	FE uncertainty	FE significance
Lumpy density	Lumpy deviation	Lumpy uncertainty	Lumpy significance

Figure D4. Density distributions extracted via the finite-element (*top*) and the two-lump lumpy (*bottom*) models for an asteroid with two counterbalancing cores. From left to right, the densities, deviations from the true density, uncertainties, and significance of the deviations are plotted. Animated form of figure 13.